PHYSICAL REVIEW A **71**, 042108 (2005)

Measurement of the parity violating 6*S*-7*S* transition amplitude in cesium achieved within 2×10^{-13} atomic-unit accuracy by stimulated-emission detection

J. Guéna, M. Lintz, and M. A. Bouchiat
Laboratoire Kastler Brossel and Fédération de Recherche, Département de Physique de l'Ecole Normale Supérieure,
24 Rue Lhomond, F-75231 Paris Cedex 05, France

(Received 9 December 2004; published 22 April 2005)

We exploit the process of asymmetry amplification by stimulated emission which provides an original method for parity violation (PV) measurements in a highly forbidden atomic transition. The method involves measurements of a *chiral*, transient, optical gain of a cesium vapor on the $7S$-$6P_{3/2}$ transition, probed after it is excited by an intense, linearly polarized, collinear laser, tuned to resonance for one hyperfine line of the forbidden $6S$-$7S$ transition in a longitudinal electric field. We report here a 3.5-fold increase of the one-second-measurement sensitivity and subsequent reduction by a factor of 3.5 of the statistical accuracy compared with our previous result [J. Guéna *et al.*, Phys. Rev. Lett. **90**, 143001 (2003)]. Decisive improvements to the setup include an increased repetition rate, better extinction of the probe beam at the end of the probe pulse, and, for the first time to our knowledge, the following: a polarization-tilt magnifier, quasisuppression of beam reflections at the cell windows, and a Cs cell with electrically conductive windows. We also present real-time tests of systematic effects and consistency checks on the data, as well as a 1% accurate measurement of the electric field seen by the atoms, from atomic signals. PV measurements performed in seven different vapor cells agree within the statistical error. Our present result is compatible with the more precise result of Wood *et al.* within our present relative statistical accuracy of 2.6%, corresponding to a 2×10^{-13} atomic-unit uncertainty in E_1^{pv}. Theoretical motivations for further measurements are emphasized and we give a brief overview of a recent proposal that would allow the uncertainty to be reduced to the 0.1% level by creating conditions where asymmetry amplification is much greater.

DOI: 10.1103/PhysRevA.71.042108 PACS number(s): 32.80.Ys, 11.30.Er, 33.55.Be, 42.50.Gy

I. INTRODUCTION: GOAL OF THE EXPERIMENT

Parity violation (PV) in stable atoms is a manifestation of the weak interaction involving the exchange of a neutral vector boson Z^0 between the electron and nucleus. It shows up in high-precision measurements testing the symmetry properties of the process of optical absorption, hence in conditions very different from those of high-energy experiments [1,2]. However, the effects in stable atoms are so small that their detection requires the choice of very peculiar conditions: i.e., the use of a heavy atom because of the Z^3 enhancement factor and a highly forbidden transition to avoid the electromagnetic interaction completely overwhelming the weak interaction. This explains why we first selected the highly forbidden $6S\rightarrow7S$ transition of atomic cesium [3] at 539 nm. In the *s* orbitals the valence electron penetrating close to the nucleus, just where the short-range weak interaction can be felt, is accelerated in the Coulomb potential associated with the nuclear charge Ze, with a strength reinforced by relativistic effects. Therefore, electron-nucleus momentum transfers of 1 MeV/*c* can occur, even though the atoms are irradiated by photons of only 2.3 eV.

In the absence of any applied electric field, the $6S$-$7S$ transition electric-dipole amplitude is strictly forbidden by the laws of electromagnetism. We measure the contribution which arises from the weak interaction E_1^{pv}. Its order of magnitude is 0.8×10^{-11} in atomic units, ea_0, instead of ~1 for the usual allowed transitions in atoms. We compare it with the $6S$-$7S$ transition electric-dipole amplitude induced by an applied electric field, βE. These measurements can be used to extract the weak charge Q_W^{expt} of the cesium nucleus via an atomic physics calculation, for comparison with the theoretical prediction Q_W^{th} of the standard model (SM) of electroweak unification theory. Thanks to the relative simplicity of the atomic structure of cesium having a single valence electron, this calculation is reliable and, owing to recent progress, its accuracy has now reached 0.5% [4–7]. Moreover, if the measurements are performed on two different hyperfine components, the results can provide a determination of the nuclear anapole moment [1,8].

The first measurements of E_1^{pv} in cesium were performed by our own group [9]. They were followed by calibrated [10], more precise ones (0.5%), achieved by the Boulder group [11,12]. Today, the latter imply no significant deviation of Q_W^{expt} with respect to the SM prediction [7]. By contrast, the reported value of the nuclear anapole moment presents serious discrepancies compared with other manifestations of parity violating nuclear forces [7,13]. Our goal is to achieve an independent measurement, as precise as possible, by a different method in order to cross-check the Boulder result. Our new approach is based on a pump-probe experiment using two collinear laser beams which operate in pulsed mode, for detection of the forbidden transition by stimulated emission. Except for the choice of the transition and the use of an applied electric field, this very different method has nothing in common with the previous PV measurements using fluorescence detection [9,11]. We validated this new approach with a 9% precision measurement in 2002. This was published in [14] where we suggested further improvements of the signal-to-noise ratio (SNR) by using

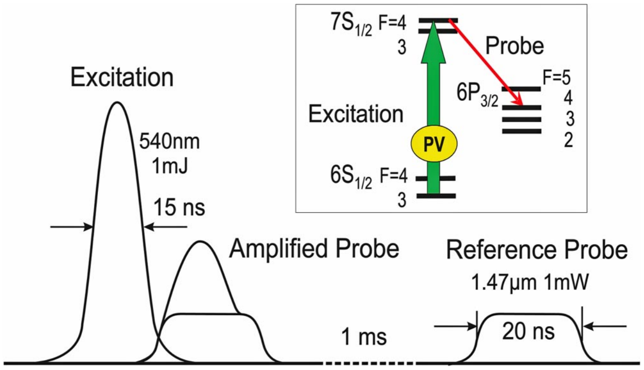

FIG. 1. (Color online) Timing of the experiment repeated for each excitation pulse ($150\ \mathrm{s}^{-1}$). Inset: ^{133}Cs levels involved ($I=7/2$, hyperfine splittings: 9.2 and 2.2 GHz in $6S_{1/2}$ and $7S_{1/2}$ respectively, 251, 201, 151 MHz in $6P_{3/2}$).

higher quality cell windows allowing better cancellation of the reflected beams [15] as well as a polarization magnifier [16]. These and additional modifications of the setup together with a tighter control of the systematic effects have resulted in a much better SNR. This paper reports on their implementation and on the subsequent measurement of E_1^{pv}, which has now reached a precision of 2.6%. It is organized as follows. In Sec. II, we describe the principles and implementation of the experiment. The recent decisive improvements of the experimental setup and their effect on the SNR are presented in Sec. III. Thereafter we describe the control and estimation of the systematic effects (Sec. IV). After a summary of the PV data acquisition and processing, we indicate how we have improved the measurement of the electric field seen by the atoms *in situ* and we present our current PV result together with consistency tests on the data (Sec. V). Finally, the implications of this kind of measurement are discussed and we conclude by considering short- and longer-term prospects (Sec. VI).

II. EXPERIMENT: PRINCIPLES AND IMPLEMENTATION

A. Detection of a chiral optical gain by stimulated emission

An intense laser pulse, tuned to resonance for one hyperfine component of the $6S_{1/2}$-$7S_{1/2}$ transition, creates, in a time interval short compared with the $7S$ lifetime (48 ns), a large population difference between the $7S$ and $6P_{3/2}$ states, which is immediately detected by a probe laser pulse tuned to resonance with one hyperfine component of the $7S_{1/2}$-$6P_{3/2}$ transition. This pulse is amplified by stimulated emission and compared with a reference pulse sent through the vapor once no more atoms remain in the $7S$ and $6P$ states. Figure 1 shows the timing of the experiment. In this way it is possible to extract the atomic contribution to the amplified probe intensity transmitted through the vapor. It is the polarization modification of the amplified probe beam which can exhibit parity violation.

An electric field $\vec{E}_l$ is applied collinear with the excitation beam. This induces an electric-dipole, "Stark" transition amplitude $E_1^{Stark}=\beta E_l$, large enough for the field to control conveniently the transition rate. The direction of $\vec{E}_l$ and the linear excitation polarization $\hat{\epsilon}_{ex}$ define two planes of symmetry of the experiment. Without any PV effect, the eigenaxes of the excited vapor would lie inside those planes of symmetry. PV actually shows up as an *angular tilt of the eigenaxes outside of those planes*. The tilt angle θ^{pv}, equal to the ratio $\mathrm{Im}\, E_1^{pv}/E_1^{Stark}$, odd under reversal of the electric field, is the relevant physical quantity to be measured, the amplitude E_1^{Stark} being determined independently (see Sec. V D). From the tilt of the optical axes, it results that the two mirror-image configurations of Fig. 2, defined by $\vec{E}_l, \hat{\epsilon}_{ex}$, and the linear probe polarization $\hat{\epsilon}_{pr}$ oriented at ±45°, are not physically equivalent: they lead to different amplification factors—i.e., to a linear dichroism on the probe transition. This PV linear dichroism is associated with the pseudoscalar $(\hat{\epsilon}_{ex}\cdot\hat{\epsilon}_{pr})(\hat{\epsilon}_{ex}\wedge\hat{\epsilon}_{pr}\cdot\vec{E}_l)$—i.e., *chiral*—contribution to the gain of the excited vapor [17].

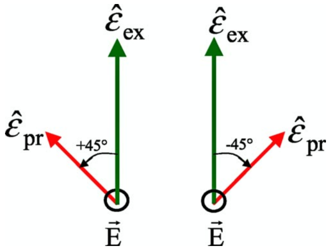

FIG. 2. (Color online) Illustration of two mirror-image configurations (left and right) that exhibit a gain asymmetry due to parity violation. The experiment is performed with either $\hat{\epsilon}_{ex} \parallel$ or $\perp$ to $\hat{\epsilon}_{pr}$ so as to yield directly the gain asymmetry (see text).

At the cell entrance the polarizations $\hat{\epsilon}_{ex}$ and $\hat{\epsilon}_{pr}$ are alternatively chosen parallel or orthogonal. Those so-called "para" and "ortho" configurations both correspond to a linear superposition of the left and right configurations leading to different optical gains (see Fig. 2). The tilt angle $\theta^{pv} \simeq 10^{-6}$ rad for $E_l=1.6$ kV/cm is measured by using a two-channel polarimeter operating in balanced mode. The probe beam is separated by a polarizing beam splitter cube into two beams polarized at ±45° of the incident polarization. The gains of the two photodetectors are adjusted in absence of the excitation beam to obtain a null signal difference, hence cancellation of the reference imbalance $[(S_1-S_2)/(S_1+S_2)]_{ref}\equiv D^{ref}$ at a level of 10^{-3} [18], with a stability ensuring absence of noise coming from compensation drifts. When the excitation pulse is switched on with $\hat{\epsilon}_{ex}$ parallel (or orthogonal) to $\hat{\epsilon}_{pr}$, we expect the PV effect to give rise to a polarimeter imbalance D^{amp}, odd under reversal of the electric field [19], since each channel measures the amplified probe intensity in either one of the two mirror configurations of Fig. 2. For each excitation pulse, the difference $D_{at}=D^{amp}-D^{ref}$ provides a direct measurement of the PV left-right asymmetry $A_{LR}\equiv D_{at}$, proportional to θ^{pv} within a proportionality factor K. It is useful to have an explicit form of this factor:

$$A_{LR}=K\theta^{pv}=2\theta^{pv}[\exp(\eta\mathcal{A})-1], \qquad (1)$$

with $\eta=11/12$ and $-11/34$ for the $7S_{1/2,F=4}\rightarrow 6P_{3/2,F=4}$ transition in the ortho and para configurations, respectively, and

$\mathcal{A}$ is the optical density for the probe. Even though this expression is valid only in first approximation (see Sec. V D and [20]), it describes well all the observed features of the amplification process. Moreover, the factor K is eliminated in the calibration procedure, allowing us to convert the *imbalance* into an absolute θ^{pv} *angle*. We achieve this by performing with a Faraday rotator an angular tilt of the excitation polarization with respect to $\hat{\epsilon}_{pr}$, of a precisely known magnitude θ_{cal} and by measuring the resulting imbalance $K\theta_{cal}$.

B. Important differences with respect to the Boulder experiment

Conceptually the present experiment [14,19,21] is very different from that of the Boulder group [11,22]. This is illustrated by a set of features summarized below.

(i) We have a direct measurement of a left-right (LR) asymmetry A_{LR} instead of a transition rate superimposed on a background of 25%.

(ii) As shown by Eq. (1) we benefit from an amplification of the (LR) asymmetry with the optical density for the probe $\mathcal{A}$ [see Eq. (1) and [20]]. As a result the parameter we measure $\mathcal{A}_{LR}$ is an increasing function of E_l instead of one falling as $1/E_l$.

(iii) We employ a longitudinal $\vec{E}_l$-field configuration instead of a transverse $\vec{E}$ and $\vec{B}$-field configuration. The absence of Stark-M_1 interference in this configuration suppresses a potential source of systematic effect troublesome in a transverse $\vec{E}$ field.

(iv) Our experiment is not limited to the two $\Delta F = \pm 1$ hyperfine components but can be extended to all of them.

(v) Our experiment is absent from line-shape distortion and line-overlap problems.

(vi) Our line-shape-independent calibration is performed continuously: the PV signal (PV alignment) is calibrated in real time by a signal of the same nature (Stark alignment [23]), as opposed to the calibration of the Boulder experiment, made difficult by incomplete line-resolution, saturation, and background effects [22].

Direct detection of an angular anisotropy in the 7S state, which ensures specificity of the signal, is obtained to the detriment of the SNR; the latter is definitely lower than that achieved in Boulder, ~1 in 10 s [11]. However, with the SNR improvement reported in this paper, the sensitivity of our pump-probe method already appears adequate for atomic PV (APV) measurements at the 1% level and we mention (Sec. VI) an extension of the method expected to improve considerably the quantum, shot-noise limit.

C. Experimental methods and setup

Table I summarizes all the parameter reversals which allow us to identify the PV signal owing to its well-defined signature. They fall into three categories: (i) the two most rapid ones, 1 and 2, allow us to isolate the LR asymmetry of purely atomic origin, $A_{LR} \equiv D_{at} = D^{amp} - D^{ref}$ via a difference performed at the millisecond time scale; (ii) the next ones, 3–5, select the E_l-odd, polarimeter imbalance behaving like a linear dichroism of the atomic vapor with axes at ±45° of the probe polarization; (iii) then, 6 and 7 exploit the invariance of the PV effect under simultaneous rotation of the excitation and probe polarizations about the common beam direction [23]. Thus, the measurements are performed in eight different configurations of $\hat{\epsilon}_{ex}, \hat{\epsilon}_{pr}$ represented in Table I lower box. An additional fast reversal, not acting on the PV signal, is the $\hat{\epsilon}_{ex}$ tilt by an angle θ_{cal}, of 1.76 mrad, required for calibrating the polarimeter imbalances. When the laser repetition rate is adjusted to 150 Hz, total completion of all these reversals takes 5 min and provides two "isotropic" determinations of θ^{pv}. Finally, after data acquisition for a period of typically 90 min, we reverse the slight tilt (~3 mrad) of the cell axis with respect to that of the laser beams (see Sec. III D below). Hence our experimental procedure provides an eightfold signature for the PV signal. More details on data acquisition and processing are given in Sec. V.

Figure 3 shows a general schematic view of the experiment. A detailed description of the various elements was presented in 1998 [21]. Since then, the important modifications we have made mainly concern the cesium vapor cells and the electric field generator. In particular, previously the cells were made of glass, with nine electrical feedthroughs and internal electrodes. They are now made of a simple alumina or sapphire tube (length 83 mm, internal diameter 10 mm) with a sapphire window glued at each end [24] and a side arm containing Cs metal. Surface conductivity of the cesiated walls is considerably lower than with cesiated glass [25], which allows us to use external electrodes [26]. Problems encountered with glass cells in our operating conditions (Cs density $\sim 10^{14}$ at/cm^3, excitation energy 1.8 mJ, $E_l \simeq 1.7$ kV/cm) were solved by such cells: (i) surface conduction currents, (ii) photoionization of Cs$_2$ dimers [27] followed by charge separation in the $\vec{E}_l$ field, and (iii) loss of transparency of the windows. The calculated field map in the external-electrode setup, together with the production of the flat-top reversible high-voltage pulses [28], is shown in Ref. [26].

However, the first signals in the sapphire cells showed the presence of unacceptable stray fields resulting from photoionization at the windows during the excitation pulse. We succeeded in reducing them by grooving circular rings on the internal surface of the wall: these prevented charge multiplication of the longitudinally accelerated photoelectrons striking the wall at grazing incidence. After this decisive step [29], significant PV measurements could start and a preliminary 9% accurate measurement validating our detection method [14] was achieved.

We now present the further decisive improvements brought to the setup since these initial measurements.

III. RECENT EXPERIMENTAL PROGRESS

A. Improvement of the excitation laser source

1. Limitations on the frequency stability coming from the reference cavity

Since our calibration procedure eliminates any dependence of the signals on the line shape, slow drifts of the excitation and probe frequencies are not a source of system-

TABLE I. Criteria and parameter reversals defining the complete PV signature, with a binary variable σ_i attached to each reversal. One elementary state of the experiment, with no parameter reversal, lasts 30 laser shots. The period of each reversal is indicated for a repetition rate of the excitation laser of 150 Hz. The sequence $(\pm\theta_{cal}, \pm E_l)$ is repeated four times before we perform reversal 4, and the sequence up to reversal 6 is repeated five times. Lower box: the eight different polarization configurations $(\hat{\epsilon}_{ex}, \hat{\epsilon}_{pr})$ used for the measurements. We indicate the polarization orientations of the excitation (large arrow) and probe (small arrow) beams.

Criteria, reversal	PV signature	Selection of	against	Nb of exc. shots	period
1) $D^{amp} = [\frac{S_1-S_2}{S_1+S_2}]^{amp}$		Polarimeter imbalance	Intensity, population	1	
2) $D_{at} = D^{amp} - D^{ref}$		Imbalance of atomic origin $\equiv$ LR asymmetry	Non atomic	1	1 ms
$\pm\theta^{cal}$ $(\sigma_{cal} = \pm 1)$	Even	Calibration imbalance		2x30	0.4 s
3) $\pm E_l$ $(\sigma_E = \pm 1)$	Odd	E_l Odd PV effect	Most PC effects (Stark-Stark)	2x60	0.8 s
4) ±tilt $\hat{\epsilon}_{pr}^{out}$ $(\sigma_{det} = \pm 1)$	Odd	True polarization effect	Instrumental defects (EMI, geometrical)	2x4x120	7 s
5) $\hat{\epsilon}_{pr}^{in} \parallel, \perp \hat{\epsilon}_{exc}$ $(\sigma_{pr} = \pm 1)$	Even	Linear dichroism of atomic origin (alignment)	Optical rotation (e.g. Faraday)	4x4x120	14.5 s
6) $\hat{\epsilon}_{exc}\{x, y\}$ 7) $\hat{\epsilon}_{exc}\{u, v\}$	Isotropic	Rotational invariant	Stray transverse $\vec{B}_\perp \& \vec{E}_\perp$ fields	4x5x (4x4x120)	5 min
8) $\pm$ tilt of cell axis $(\sigma_\psi = \pm 1)$	Even	Incident excitation beam	Back-reflected excitation beam	$\sim 10^6$	90 min

4 $(\hat{\epsilon}_{exc}, \hat{\epsilon}_{pr})$ $\parallel$ & $\perp$ configurations

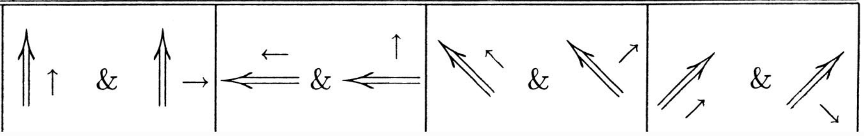

atic error. However, it is important that the lasers stay at resonance to preserve the optimum of the SNR, particularly in a PV experiment where the data acquisition lasts over long periods of time.

The probe beam frequency is stabilized on a hyperfine component of the $7S$-$6P_{3/2}$ transition, using polarization spectroscopy in an auxiliary Cs cell in which a discharge continuously populates the $6P_{3/2}$ level. An analogous method is not possible on the forbidden $6S$-$7S$ transition. The excitation frequency is stabilized on an external Fabry-Perot cavity (FPC). The FPC is tuned at resonance for the $6S_{F=3} \rightarrow 7S_{F=4}$ transition using dispersion-shaped signals provided by the pump-probe PV setup itself, either optical rotation, by temporarily making the excitation beam circularly polarized (case of the $6S_{F=3} \rightarrow 7S_{F=4} \rightarrow 6P_{3/2,F=5}$ transition) or birefringence, by temporarily making the probe beam circularly polarized (case of the $6S_{F=3} \rightarrow 7S_{F=4} \rightarrow 6P_{3/2,F=4}$ transition). This allows us to tune initially the excitation frequency and then control it at regular time intervals. Although the vessel containing the reference FPC is evacuated and temperature

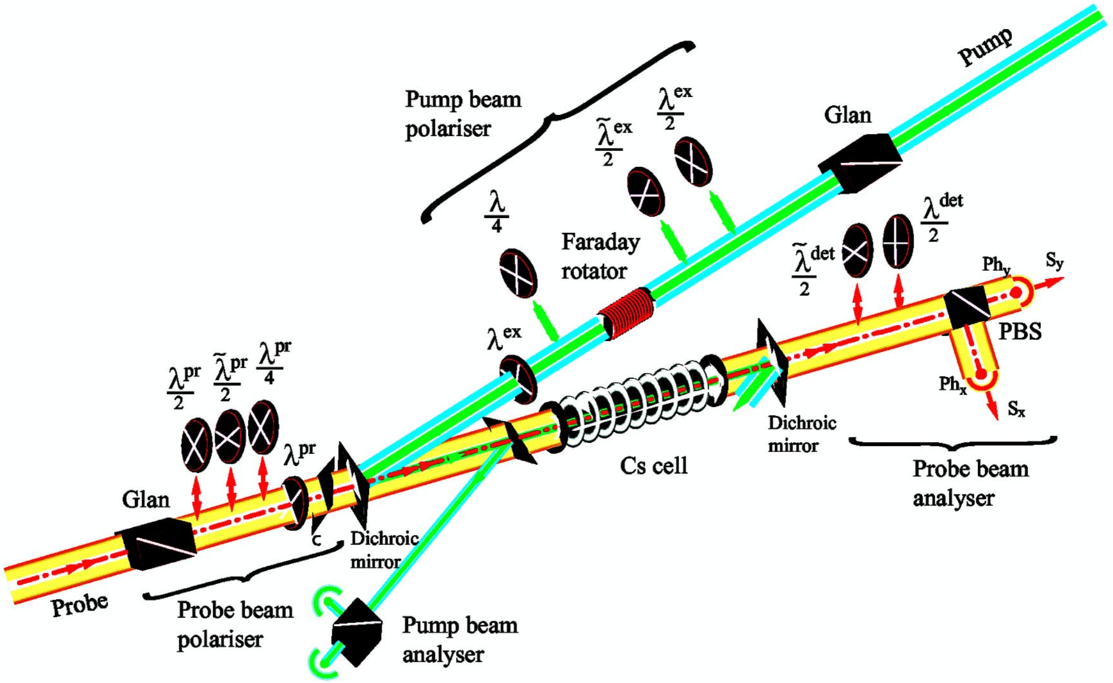

FIG. 3. (Color online) Schematic view of the experiment. $\lambda/2,\tilde{\lambda}/2,\lambda/4$: insertable half- and quarter-wave plates for controlling the pump and probe polarizations (superscript ex and pr, respectively). $\lambda/2$ and $\tilde{\lambda}/2$ allow for reversals 6 and 7 in Table I, respectively. The $\lambda/4$ are used when circular polarization is required for initial frequency tuning of the pump beam. λ: tilted wave plates for birefringence compensation. $\lambda^{det}/2$: performs reversal 4 in Table I. $\tilde{\lambda}^{det}/2$: restores the probe when input $\tilde{\lambda}^{pr}/2$ is inserted. PBS: polarizing beam splitter cube with axes at ±45° of axes x,y (polarimeter analyzer). The pump beam analyzer performs analogous role for the pump beam. Ph_x,Ph_y: InGaAs photodiodes, providing the polarimeter signals S_x,S_y, respectively (S_1,S_2 in text). Dichroic mirror: dielectric mirrors reflecting the pump $(R>99.9\%)$ while transmitting $\sim$95% of the probe. Glan: Glan-air polarizer. C: glass plate to compensate linear dichroism. Cs cell: cell with external ring electrodes.

stabilized, the excitation laser frequency drifts by typically a few megahertz per minute. We first used a correction procedure assuming a linear drift, but the slope was not constant enough for the approach to be reliable. To do better we stabilized the reference cavity on an iodine molecular line.

2. Long-term frequency stabilization of the cavity on a $^{127}I_2$ line

By observing the fluorescence of iodine in the region of interest and by using the theoretical spectrum of $^{127}I_2$ given by the program IODINESPEC [30] supplied by Toptica, we found that the line the closest to the $6S_{F=3}\rightarrow 7S_{F=4}$ hyperfine transition was the very weak hyperfine component (a15) belonging to the $J''=36$, $\nu''=1\leftarrow J'=37$, $\nu'=31$ rovibrational transition [37 P (31-1)], the actual frequency difference being $\Delta\nu\simeq -300$ MHz. The method of saturation spectroscopy is required to resolve the hyperfine lines of I_2. A long iodine cell (50 cm) is necessary to increase the absorption signal and saturation effects are enhanced by focusing the laser beams into the cell with 30-cm focal lenses.

A fraction of light (13 mW) is taken from the 539-nm cw dye laser (before its pulsed amplification; see Sec. III A 3 below) and enters the setup through a polarizing beam splitter cube, as schematized in Fig. 4. A large fraction of this beam—i.e., the pump—is passed twice through an acousto-optic modulator (AOM1), shifting the frequency by $\Delta\nu_1=$

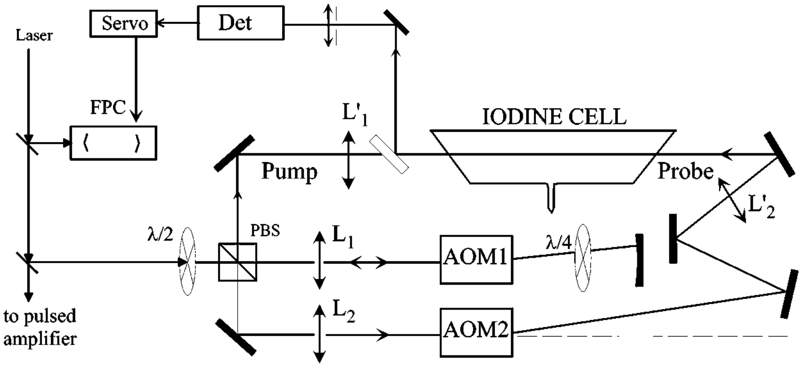

FIG. 4. Experimental setup for excitation-laser frequency stabilization by saturation spectroscopy of I_2. FPC: reference Fabry-Perot cavity. PBS: Polarizing beam splitter cube. AOM 1, 2: acoustooptical modulators.

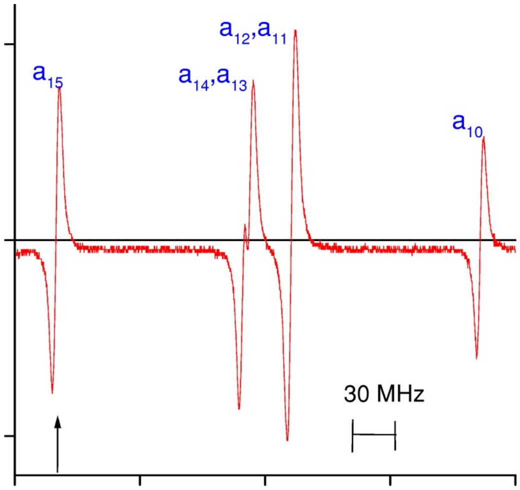

FIG. 5. (Color online) Iodine saturation-spectroscopy signal used to stabilize the reference Fabry-Perot cavity, obtained with the setup shown in Fig. 4. The arrow indicates the hyperfine transition 37 P (31-1) of $^{127}I_2$ used for locking on the $6S_{F=3} \rightarrow 7S_{F=4}$ transition.

-2×200 MHz. A small fraction of it (the probe) is passed through a second acousto-optic modulator, AOM2, shifted in frequency by $\Delta\nu_2 \sim -200$ MHz and superposed with the pump in the I_2 vapor along a counterpropagating path. The saturation spectroscopy signal appears when the sum of the laser frequency ν_{laser} and $\frac{1}{2}(\Delta\nu_1+\Delta\nu_2)$ is resonant with the iodine vapor. To achieve enough sensitivity, a frequency modulation (amplitude 2.0 MHz, modulation frequency 19 kHz) is superimposed on $\Delta\nu_1$. Then, by lock-in detection of the transmitted probe intensity at the pump modulation frequency, we can observe the derivative of the absorption signal. This symmetric dispersion-shaped signal (Fig. 5) is used as an error signal in a feedback loop ensuring long-term stabilization of the external FPC to the center of the hyperfine $6S_{F=3} \rightarrow 7S_{F=4}$ Cs transition after initial $\Delta\nu_2$ adjustment. In this way, frequency drifts are suppressed (i.e., smaller than the cw laser spectral width ~1 MHz) without interruption of the PV data acquisition, over periods as long as several hours. Note that the use of two AOM's is very helpful, since it ensures excellent rejection of any Doppler background and absence of stray light modulated at the signal frequency without requiring the use of a reference beam, most often subjected to drifts.

At the beginning of a PV data acquisition, the shift $\Delta\nu_2$ is adjusted so as to maximize the probe amplification in the cesium cell or, for higher sensitivity, to cancel out the relevant dispersion-shaped signal. Because of the ac Stark shift $\Delta\nu(i_{ex})$ induced by the excitation laser, the value of the adjusted shift $\Delta\nu_2$ depends on the excitation energy i_{ex}: $\Delta\nu_2(i_{ex})=-2\Delta\nu(i_{ex})$, since $\Delta\nu_1$ is kept fixed. The ac Stark shift is shown in Fig. 6. Since the excitation and probe pulses overlap, the intense excitation pulse shifts both the excitation and probe transition frequencies, by $\Delta\nu_{ex}$ and $\Delta\nu_{pr}$, respectively. In our operating conditions, $\Delta\nu_2$ is thus a linear combination of both shifts. Whatever the value of i_{ex}, the probe laser frequency remains locked to the atomic transition observed in a reference cesium cell where the excitation beam is absent. Consequently, in the presence of the excitation beam, the probe beam is no longer resonant for the atomic zero-velocity class, but becomes resonant for atoms of velocity $c\Delta\nu_{pr}(i_{ex})/\nu_{pr}$. The maximum of amplification occurs when the excitation beam is resonant with that same velocity class. The laser shift required to be at resonance is then $\Delta\nu_{laser}(i_{ex})=\Delta\nu_{ex}(i_{ex})-(\nu_{ex}/\nu_{pr})\Delta\nu_{pr}(i_{ex})$. Hence, the shift of $\Delta\nu_2$ accompanying the i_{ex} variations is interpreted as

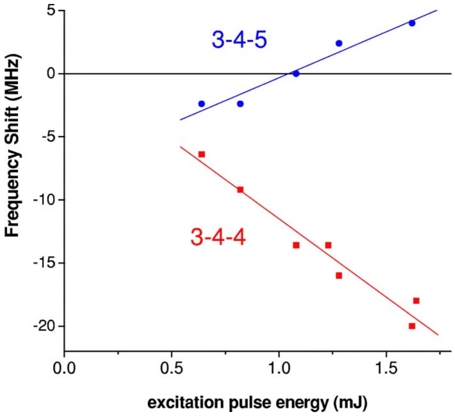

FIG. 6. (Color online) ac Stark shifts $\Delta\nu(i_{ex})$ induced on the $6S_{F=3} \rightarrow 7S_{F=4} \rightarrow 6P_{3/2,F'}$ resonance vs the excitation energy i_{ex}, deduced from the shift of AOM2 in the iodine setup of Fig. 4 (see text). Temporal pump-probe overlap: 10 ns. The origin on the vertical axis is chosen arbitrarily and is different for both transitions.

$$\Delta\nu_2(i_{ex}) = -2\Delta\nu_{ex}(i_{ex}) + 2\frac{\nu_{ex}}{\nu_{pr}}\Delta\nu_{pr}(i_{ex}). \qquad (2)$$

Since $\nu_{ex}/\nu_{pr}=2.72$, we note the large sensitivity of $\Delta\nu_2(i_{ex})$ to the ac Stark shift of the probe transition.

At first sight the large ac-Stark-shift *difference* between the two hyperfine lines shown in Fig. 6 might look surprising. Actually an *additional* ac Stark shift, of opposite sign, is induced by the probe beam when it is amplified during propagation through the vapor, the proportionality to i_{ex} resulting from the amplification. After a careful study, out of the scope of this paper, we have found that this effect, greater for the 3-4-5 system than for the 3-4-4 one which has a probe gain twice smaller, explains the overall Stark-shift difference.

3. Improvement of the spatial profile of the pulsed beam

The beam delivered by the cw dye laser is pulsed amplified by passing through a commercial system (Lambda Physik FL 2003) with three rectangular cells through which circulates a dye solution (Coumarin 153 in Methanol) pumped by a XeCl excimer laser (18-ns-long pulses, 100 mJ at 308 nm) at a maximum repetition rate of 200 Hz. With transverse pumping, optical alignments necessary to obtain the desired ideal circular spatial profile of the beam proved to be rather critical. We have tried for the last amplifier to use a Bethune cell which ensures pumping with cylindrical symmetry. A nice circular shape was obtained, but only at repetition rates below 30 Hz. Beyond this rate, an unacceptable jitter of the beam position attributed to the turbulence of the

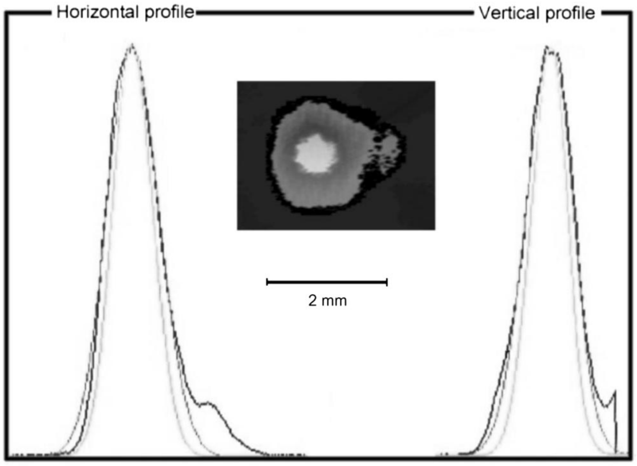

FIG. 7. Spatial profile of the excitation beam. Inset: typical image of the beam transverse section obtained with the charge-coupled-device (CCD) camera analyzing a fraction of the beam at the input of the Cs cell. Integrated profiles along *x* and *y*, horizontal and vertical axes, respectively. Dark line: measured profile. Gray line: Gaussian fit with beam waist radius of 0.90 mm. Light grey line: for comparison, probe beam Gaussian profile of radius 0.70 mm.

liquid flowing through the cell forced us to abandon. Trying back the rectangular cell with the dye circulator dedicated to the Bethune cell, a more powerful one with an adjustable flow rate [31], we could obtain a stable circular profile at repetition rates up to 180 Hz, with only little dependence on the day-to-day realignments and on the aging of the dye-solution. Figure 7 illustrates such a typical profile.

B. Increasing the probe-beam extinction ratio

1. Motivations

The optical switch which produces 20-ns-long optical pulses from the continuous probe-laser source at 1.47 μm is a key component of the set up. It turns out that the noise performance of our detection method depends crucially on its extinction ratio. This integrated device [32] driven by low voltages has rapid rise and fall times ($\leqslant 1$ ns) and its extinction ratio is usually as low as 10^{-3}. But probably due to humidity changes, occasionally it rises to several times 10^{-3}, rendering reliable measurements impossible. Indeed, the leakage photons going through the "closed" optical switch continue to probe the Cs vapor. They participate in the detected signal for the time characteristic of the photocurrent integration operated by the dual detection chain at each probe pulse [33]. Since the $6P_{3/2}$ state, of the 5 μs effective lifetime due to resonance radiation trapping, is progressively populated in the early stages of deexcitation of the vapor [34], the time-integrated probe intensity undergoes a prohibitively large absorption. The base line of the charge integrated pulse (20-ns rise time followed by a 50-μs exponential decay) becomes distorted and fluctuates. This causes noise that is not completely filtered out by the Gaussian pulse shaper (adjusted with $\tau_i = \tau_d = \tau = 1$ μs for optimal noise rejection [33]). To prevent noise blasts due to the unpredictable behavior of the optical switch, we installed a Pockels cell in series with it.

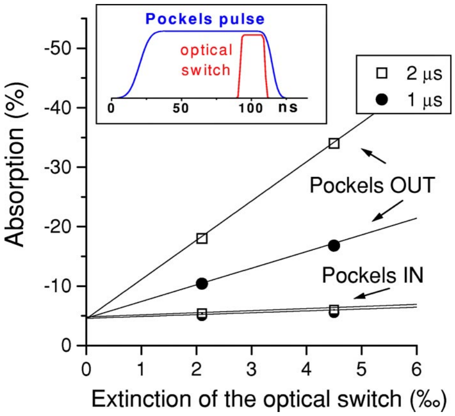

FIG. 8. (Color online) Reduction of the probe-beam absorption thanks to the Pockels cell for two values of the time constant of the Gaussian pulse shaper, $\tau = 1$ and 2 μs. Inset: timing of the light pulses produced by the Pockels cell and by the optical switch.

2. Operating conditions of the Pockels cell and the optical switch

We placed the Pockels cell (PC) right at the input of the optical switch (OS). This provides the advantage of reducing considerably the periods of illumination of the OS, probably a wise protection against possible photocreation of color centers in the integrated waveguides. The transmission is 91% and the extinction ratio 0.4%. The PC is driven by a fast pulse generator (fall and rise time of about 20 ns, minimum pulse duration 100 ns [35]). As shown in the inset of Fig. 8, the beam is let through ~80 ns before the OS opens but it is interrupted shortly after the OS closes. Figure 8 also illustrates the effect of the PC on the absorption measurements. We plot the measured absorption with or without the PC versus the extinction ratio of the OS, varied at will by changing the driving voltage. When the PC is operated, the probe absorption is considerably reduced and the initial dependences on both the extinction ratio of the OS and the time constant of the shaper disappear.

3. Trigger system for synchronized operation of the cell and the switch

The synchronisation of the whole system presented a technical difficulty because the first probe pulse amplified by the vapor is followed by four reference probe pulses separated in time by about 1 ms, for making negligible the photon shot noise on the reference measurements. It is important that the shape of the reference pulses be identical to that of the first probe pulse. This requires excellent synchronization between the pulses which drive the Pockels cell and the optical switch. On the other hand, the first probe pulse must be triggered by the excimer laser driving the excitation pulse so as to avoid a temporal pump-probe jitter (~5 ns shot-to-shot fluctuation of the excimer laser thyratron). The triggering system implemented is sketched in Fig. 9. It has two differ-

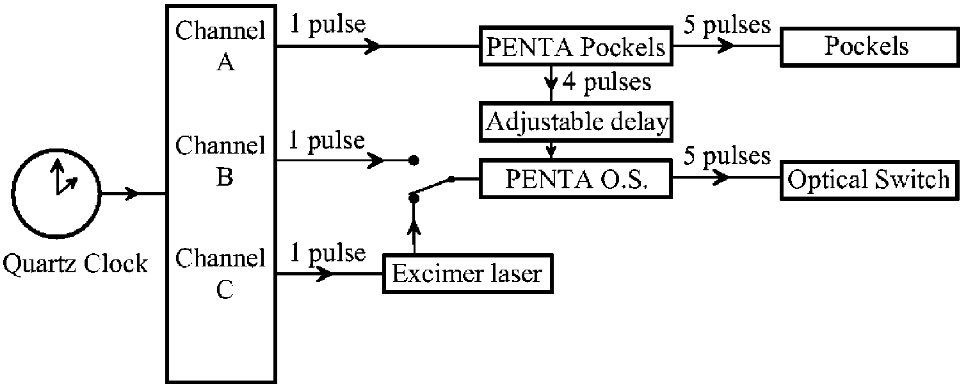

FIG. 9. Scheme of the electronic circuitry feeding five synchronized trigger pulses to drive the Pockels cell ("Penta Pockels") and the optical switch ("Penta OS") at each amplified pulse followed by four reference pulses. Each channel (A, B, C,…) has an adjustable delay.

ent operating modes, one requiring operation of the excimer system, the other, which does not, being used for preliminary procedures (probe beam alignment and polarimeter adjustment).

C. Birefringence-free polarization-tilt magnifier

1. Principle of polarization-tilt magnification

In an earlier work [16], we suggested using a dichroic component to amplify the tilt angle acquired by the probe beam after its passage through the excited vapor. The idea is simply to transmit differently the polarizations along two orthogonal directions, the direction of the incoming beam and the orthogonal direction. In this way we can attenuate the polarization parallel to the incoming probe polarization, while letting through the orthogonal polarization which carries the important information—i.e., the tiny component resulting from the tilt induced by the vapor.

Let us suppose that $\hat{x}$ is the incoming probe polarization and that the transmission coefficients of our dichroic device for the amplitude of the field are $t_x=0.5$ and $t_y \simeq 1$ in the two eigendirections $\hat{x}$ and $\hat{y}$. It is seen easily that after passage through this device, the angle between the light polarization and the $\hat{x}$ direction is multiplied by 2. The light intensity reaching each detector is divided by 4. Such a "polarization magnifier" does not automatically lead to an increase of the SNR. In the shot-noise limit, we cannot expect any SNR improvement, except if we increase the intensity of the probe beam at the input of the cell provided that the asymmetry amplification is not damped under the effect of saturation by the probe beam intensity [36]. Actually the power of our color center laser can be increased by a maximum factor of $\sim$2.5. With the 1.5 mW power then available in the Cs cell (100 mW at the output of the laser), saturation effects for the probe transition $7S_{F=4}-6P_{3/2,F=4}$ the best suited to PV measurements remain small, as expected [36]. If photon shot noise is dominant, the SNR expected improvement is $\sqrt{2.5}$, which was worth a try.

We note that the magnifier plays the same role as the "uncrossed polarizer" in the quasiextinction method of polarimetry. Thereby, this dichroic element allows us to combine the advantages of two well-known operating modes of polarimetry: quasiextinction mode and balanced mode. In the former, intensity noise is reduced by optimizing the uncrossing angle, while the latter allows one to suppress all common-mode noise.

2. Realization

Initially, we considered the possibility of using a single plate with a dichroic multilayer coating [16,37], but this solution suffered from problems linked with the large, incidence-dependent, birefringence of the coating. We finally turned to a stack of four or six silica plates at Brewster incidence. This arrangement yields the required magnification factor ($\sim$2 or 3) and birefringence is acceptably small provided that interference between multiple reflections is suppressed by using wedged, tilted plates, so that no two surfaces are parallel [38].

As explained previously, the polarization of the incoming probe beam at the cell entrance determines the polarization direction that has to be attenuated before reaching the polarimeter. For practical reasons, the device operates in a fixed position, with the incidence plane vertical. Nevertheless, we can use it in any of the four possible directions of the probe polarization, thanks to two additional half-wave plates which restore the polarization direction before the magnifier.

We have found that the device with either four or six plates operates satisfactorily with very stable characteristics. Without the magnifier, the calibration left-right asymmetry for a tilt θ_{cal} of $\hat{\epsilon}_{ex}$ with respect to $\hat{\epsilon}_{pr}$ is compatible with the expected value $2\theta_{cal}[\exp(\eta\mathcal{A})-1]$ [Eq. (1)]. With the magnifier in position, the measured left-right asymmetry is amplified with respect to that value by the expected factor t_y/t_x, for the eight pump-probe configurations. As to the gain in SNR, we estimate it to be about 1.5–2 with the four-plate device, hence barely larger than what we could expect in the shot-noise limit. The six-plate device improves this result slightly, by at most 20%. This last result is easily understood were shot noise dominant in our operating conditions: (i) since we could not increase the input intensity sufficiently to compensate for the twice higher attenuation factor ($t_x^2 \approx 1/8$ instead of $1/4$), the small intensity-independent contribution of noise increased accordingly, and (ii) for the larger probe beam intensity required for better efficiency of the device, atomic saturation started to show up on the asymmetry amplification.

Finally, we mention other improvements on the probe beam part of the experiment. Residual étalon effects inside the polarimeter have been canceled out. The short-term stability of the servo loop used to stabilize the probe laser frequency has been improved. Since the detected probe flux is lower when the magnifier is in use (even though the incoming probe intensity is higher), we have increased the gain of the charge-integrating preamplifiers by changing the input capacitor from 7 to 4 nF, so as to use the whole dynamic range of the detection chain.

D. Control of the beam reflection at the cell windows

Due to the high refraction index of sapphire ($n=1.77$), reflection of the input laser power at each window is about 15% and can be a source of losses on the 7*S* excited atom density (reflection at the entrance window) or of uncontrolled contributions (reflection at the output window). One might also worry about interferences taking place *between* the two windows which are precisely mounted, normal to the cell axis (tilt less than 1 mrad).

1. Interferences inside and between the windows: Source of noise

Important progress has been achieved with the realization of the extinction of the excitation beam reflected by the windows. Depending on its parallelism, any cell window behaves more or less as a temperature-tunable Fabry-Perot étalon [15]. In the very first cell used for measurements, imperfect parallelism prevented us from obtaining a reflection coefficient lower than $\simeq 5\times 10^{-2}$. An interference pattern was distinguishable in the reflected beam profile, with a contrast and intensity varying with the position of the beam impact and with the incidence. We also observed that tuning the window temperature at a reflection *maximum* ($R_{max} \simeq 20\%$) caused an increase of noise. All the subsequent cells were fabricated [24] with windows made by Meller Optics [39] with both an excellent parallelism (better than 10 μrad over the 6-mm-diam central region) and very good [0001] crystal axis orientation (defect on *C*-axis orientation $\leqslant 0.5°$, birefringence $\leqslant 2\times 10^{-3}$ for a 0.5-mm-thick window). As expected, we clearly observed a reduction of the noise when the reflection was reduced to a few times 10^{-3} per window thanks to temperature stabilization (to 0.1 °C), achieved independently for each window.

Given the window thickness, we obtain successive reflection minima at 540 nm by shifting the temperature by successive intervals of 14 °C while the FSR corresponds to 40 °C at the probe wavelength. Hence, we cannot expect to obtain reflection extinction of comparable quality simultaneously at both wavelengths. However, by varying the operating point by increments of 14 °C over a wide acceptable temperature range (210–270 °C) one can choose an operating temperature which provides the best probe transmission with excellent reflection extinction for the excitation beam. In a majority of cells we could obtain a $\approx$95% probe transmission leading to a further improvement of the observed SNR. This is likely to result from the quasisuppression of the interference between the probe beams reflected at the input and output windows. No systematic effect is expected from this interference, due to the way we process and calibrate the PV data. As a result of drifts in the interference order, however, we do expect noise associated with temperature drifts of the cell body, even though cell windows are accurately stabilized. The smaller the amplitude of this interference, the smaller the associated noise.

2. Tilt-odd effect: Interpretation and suppression

When the probe beam is at normal incidence to one of the windows, we observe an excess of noise in the polarimeter signals, making precise measurements impossible. Although the ideal configuration requires perfect alignment of both laser beams along the cell axis, we have to concede a small tilt of the cell axis with respect to the beams ($\psi \sim 3$ mrad). Since such a tilt breaks the symmetry, we reverse its sign after about 90 min of data acquisition, and we average the results obtained with both tilts, affected in practice by similar statistical noise. The reversal $\psi \leftrightarrow -\psi$ is performed by tilting the oven containing the cell while keeping the position of the beams unchanged. We now justify this procedure which suppresses a possible systematic effect. (An overview of the systematics is given in Sec. IV.)

In Ref. [23] [Sec. 4.4, Eq. (39)], we showed that a misorientation of the probe beam with respect to the excitation beam generates a second-order systematic effect on the measurement of θ^{pv} for a given direction of $\hat{\epsilon}_{ex}$:

$$\theta_{syst}(\hat{\epsilon}_{ex}) = \frac{E_t^+}{E_l}[\hat{k}_{ex} \wedge \hat{k}_{pr} \cdot \hat{E}_t^+ - (\hat{k}_{ex} \wedge \hat{k}_{pr} \cdot \hat{\epsilon}_{ex})(\hat{E}_t^+ \cdot \hat{\epsilon}_{ex})]\, \hat{z} \cdot \hat{E}_l, \tag{3}$$

involving the alignment defect $\hat{k}_{ex} \wedge \hat{k}_{pr} = \delta\alpha \hat{n}$ and the transverse E_t^+ field defect even under the longitudinal field reversal, both to first order. In our experiment the pump-probe alignment of the two beams is adjusted precisely enough, using a four-quadrant cell, to avoid any really significant contribution. However, a problem can arise from the portion of the excitation beam *back-reflected* by the output window, which is misaligned with the probe beam. Let us denote by $\hat{k}'_{ex}$ the reflected beam direction and $\hat{n}$ the direction such that $\hat{k}'_{ex} \wedge \hat{k}_{ex} = 2\psi\hat{n}$, where ψ is the angle of incidence. We see that a contribution, linear in ψ, appears in $\theta_{syst}(\hat{\epsilon}_{ex})$ [Eq. (3)] that does not average to zero in the "isotropic" value—i.e., the average after 90° rotation of $(\hat{\epsilon}_{ex}, \hat{\epsilon}_{pr})$, [23]:

$$\langle \theta_{syst} \rangle_{\hat{\epsilon}_{ex}} = \psi R \frac{E_t^+}{E_l}(\hat{n} \cdot \hat{E}_t^+)\, \hat{z} \cdot \hat{E}_l, \tag{4}$$

where R is the reflection coefficient of the output window. It simulates the PV effect, except that it is *odd* under the $\psi \leftrightarrow -\psi$ reversal. We have neglected the loss of detection efficiency due to the incomplete overlap of the probe beam and reflected excitation beam since, for $\psi = 3$ mrad, the beam separation is only 0.5 mm at the entrance of the cell, which is less than the probe beam radius of 0.7 mm.

With $R=0.10$, a typical value for standard sapphire ($n=1.77$) windows, taking $\psi=3$ mrad and $E_t^+/E_l = 3\times 10^{-3}$, using Eq. (4) we predict $\langle \theta_{syst} \rangle_{\hat{\epsilon}_{ex}} = 0.9$ μrad. This reduces to 0.02 μrad for good windows with $R=0.002$. For larger tilts, the overlap of the probe and reflected excitation beams is partial and the ψ-odd contribution [Eq. (4)] is not expected to grow linearly, but actually to saturate. Indeed, this corresponds to our observations when the tilt is increased up to $\psi \sim 5$ mrad.

In conclusion, the tilt-odd effect could correspond to a source of systematic effect if there were no means to suppress it. Actually, we have two ways to reduce this effect efficiently: (i) by reducing the reflection coefficient to the 10^{-3} level and (ii) by reversing the sign of ψ. The most convenient way to perform the tilt reversal of the cell axis with respect to the unchanged common beam direction is to rotate the cell around a vertical axis passing through its center. The displacement of the beam impact on each window is only 240 μm. On such a small scale, the value of E_t^+ is not expected to change, which is in fact confirmed by our control of the transverse fields. This is important for efficient suppression of this effect.

We want to mention a second source of tilt-odd effect. In [23] we analyzed the systematic effect generated by the combined action of the transverse electric and magnetic field components E_t^- and B_t^-, both odd under reversal of the longitudinal field. By tilting the cell, together with the electrodes assembly [26], we produce an electric component, $E_t^- = \psi E_l$, and hence a ψ-odd systematic effect. Using Eq. 34 of Ref. [23], we obtain the new isotropic contribution to $\langle \theta_{syst} \rangle_{\epsilon_{ex}}$:

$$\langle \theta_{syst} \rangle_{\epsilon_{ex}} = (\hat{z} \cdot \hat{E}_l)\psi \omega_{F'} \tau (\hat{E}_t^- \cdot \hat{B}_t^-).$$

For typical values of B_t^- less than 2 mG (leading to a Larmor precession angle of $\omega_{F'}\tau \leqslant 40$ μrad) and $\psi = 3$ mrad, we obtain $\langle \theta_{syst} \rangle_{\epsilon_{ex}} \leqslant 0.12$ μrad. Thanks to the suppression of $\langle \theta_{syst} \rangle_{\epsilon_{ex}}$ in the $\psi \leftrightarrow -\psi$ reversal, we can consider this effect to be harmless.

E. Cesium cell with electrical continuity between the inner and outer sides of conductive windows

The last improvement consisted in our using sapphire windows covered with a niobium, 2-μm-thick, coating deposited over a thin layer of titanium, except for the 6-mm central region left uncovered for the laser beams. This type of coating allows one to control better the electric field near the windows, since the HV potential can be applied *inside* the cesium cell by direct contact with the *outer* part of the metal coating. By comparison with what happens when the window potential is floating, the electric charges left at the windows as a result of photoionization are more efficiently compensated by those supplied by the generator maintaining the potential fixed.

The vacuum-tight gluing of such coated windows to the alumina tube, under vacuum to prevent the coating from oxidation, was implemented by Sarkisyan and co-workers [40].

In this last cell we have obtained the best SNR, corresponding to a further ~15% improvement.

A measurement method relying on atomic signals (described in Sec. V D) has allowed us to determine precisely the electric field experienced by the atoms inside the cell. It is interesting to compare the measured value E_l^{expt} with the magnitude E^{nom} expected from the numerical simulation taking into account the geometry of the electrode assembly and the potential distribution (for details see [26]). The results exhibit a marked difference between the cell having electrically conductive windows, where we find $E_l^{expt}/E^{nom} = 0.98 \pm 0.01$, and a cell with uncoated windows, leading to $E_l^{expt}/E^{nom} = 0.92 \pm 0.01$. The simulation does not take into account the distribution of electric charges inside the cell resulting from the photoionization at the windows. Accounting for this process, the observed variation of E_l^{expt}/E^{nom} from one type of cell to the other is not surprising: photoemission leaves a positive surface charge at the cathode window, and the accelerated electrons accumulate at the anode window, giving rise to a negative surface charge. Applying the potential, via the coatings, at the inside surface of the windows contributes to screening the effect of the surface charges in the vapor. In addition, the photoelectrons that reach the anode window at the periphery are evacuated through the coating. The applied electric field is then expected to be closer to the calculated electrode field.

F. Net observed improvement of the S/N ratio

After this set of improvements (Secs. III A–III E) compared to our initial runs reported in [14], the average value of the standard deviation per isotropic value of the calibrated E_l-odd linear dichroism (see Sec. V A) has been reduced by a factor of 2.6 (initially 5.1 μrad and now 2.0 μrad) while the repetition rate has been increased from 90 to 160 Hz. All in all, the SNR for a one-second-measurement time has been increased by a factor of ~3.5; hence, *the averaging time required to reach a given statistical accuracy is reduced by a factor of* ~12, and this without introducing new systematic or spurious effects.

Even so, this does not correspond to a technological limit: for instance, the same kind of pulsed laser we are using has been operated at a repetiton rate reaching 400 Hz [41]. This would provide another improvement by a factor of ~1.5, provided that the pointing stability of the excitation beam can be preserved when the repetition rate is doubled.

We have already discussed the noise-equivalent angle and shown [16,42] that, for a given number of incident probe photons, n_{in}, the quantum-noise-limited SNR per excitation pulse,

$$S/N = \theta^{pv} \sqrt{n_{in}} \mathcal{A}_{av} \exp(\mathcal{A}_{av}/2),$$

is a rapidly growing function of the optical density averaged over the para and ortho configurations, $\mathcal{A}_{av} = (\mathcal{A}_{\parallel} + \mathcal{A}_{\perp})/2$. Actually our measurements show an excess of noise with respect to the shot-noise limit by a factor of 1.5–2. Even so, while making the various improvements of our experiment, we have checked that the mechanism of asymmetry amplification by stimulated emission is in practice a definite source of improvement of the SNR. The optical density involves the number of excited atoms in the vapor column through which passes the probe beam, N_{ex}. The latter is proportional to E_l^2 and to the excitation intensity. We have increased those parameters, though without overstepping the limits beyond which new sources of noise might arise. This is especially important when we increase the electric field (see Sec. V B our diagnosis of noise at short time scale). In practice, for the $6S_{F=3} \rightarrow 7S_{F=4} \rightarrow 6P_{3/2,F=4}$ transition, good measurement conditions were achieved with typical values of the asymmetry A_{LR}/θ of 1.2 (0.6), at optical densities $\mathcal{A}$ of 0.5 (1.0) in the ortho (para) configurations.

IV. CONTROL, REDUCTION, AND ESTIMATION OF THE SYSTEMATIC EFFECTS

In this section, we present an overview of the origins of the systematic effects and the means we adopted to reduce and estimate them (to the exception of the tilt-odd effects considered in Sec. III D). The order chosen in this presentation corresponds to decreasing order of importance played by each effect.

A. Longitudinal magnetic field odd under reversal of $\vec{E}_l$

We have observed a longitudinal magnetic field odd under reversal of $\vec{E}_l$, dubbed the B_z^- field. Its likely origin is the motion of electric charges following the photoionization process which may have a small helicity around the propagation axis. The B_z^- field gives rise to an E_l-odd Larmor precession of the axes of the parity conserving linear dichroism, thus simulating the PV tilt angle. Even in a field as small as $B_z^- = 50$ μG, the precession is of the same order of magnitude as θ^{pv}.

We measure this field by observing the optical rotation, *odd* under $\vec{E}_l$ reversal, that it generates by a simple Faraday effect [43]. This control is performed by selecting a hyperfine component of the probe transition particularly sensitive to a magnetic field. The Faraday effect on the $7S_{F=4} \rightarrow 6P_{3/2,F=5}$ line is 10 times larger than the linear dichroism resulting from the Larmor precession of the excited-state alignment which might simulate APV. In order not to rely on the temporal stability of the value of B_z^- during long acquisition times, the measurement is made before and after the PV data taking. At regular intervals the calibration factor for the Faraday effect is obtained by applying a "large," known, magnetic field. This is also done on the $7S_{F=4} \rightarrow 6P_{3/2,F=4}$ probe transition for the calibration factor of the dichroism precession. Thus the measured value of θ^{pv} can be corrected for reliably and accurately. Both the sign and magnitude of the B_z^- field varied from one cell to another. In the best cases, the correction remained at the level of a few percent of the PV effect, while it was of the same order of magnitude in two cells (cells Nos. 5 and 6). The time devoted to B_z^- measurements varied from 30% to 60% of the total data acquisition time. It was chosen so that the error associated with the resulting correction on θ^{pv} remained small compared to the statistical accuracy of the PV measurement.

B. Effects resulting from a breaking of the cylindrical symmetry

Particular attention has been given to the defects that break the cylindrical symmetry of the setup, such as the transverse $\vec{E}$ and $\vec{B}$ fields and misalignment of the two beams. Our study [23] has shown that for the polarimeter imbalance to be altered in a way which simulates θ^{pv}, *two defects* are necessary. Some of the systematics ("class 2" systematics in [23]) average to zero when the two polarizations $\hat{\epsilon}_{ex}, \hat{\epsilon}_{pr}$ are rotated together by 45° increments around the common beam direction. The really serious effects ("class 1") are those that do not average to zero under this operation. They all require the presence of a transverse electric field.

TABLE II. Means of reduction of the E_l-odd and the E_l-even components of the transverse $\vec{E}_t$ and $\vec{B}_t$ fields.

Defect	Origin	Reduction
E_t^-	Tilt of the cell	$(\psi/-\psi)$ mean tilt
E_t^+, B_t^-	Photoemitted charges [29]	Cell translation $\perp \vec{E}_l$
B_t^+	Residual ambient field	Compensating coils

These "class 1" effects have two different origins.

(1) Pump-probe misalignment of angle $\delta\alpha\hat{n} = \hat{k}_{ex} \wedge \hat{k}_{pr}$. This misalignment gives rise to a systematic effect on the measurement of θ^{pv} by its coupling to an E_t^+ electric field, even under E_l reversal. Our method to minimize this effect is (i) to superpose the pump and probe beams, on the *same centering device*, at the input and output of the cell (see Sec. 3.3 in Ref. [21]), and (ii) to measure the transverse E_t^+ field (procedure in next section), and then slightly translate the cell transversally along x or y so as to reduce it to the level of $\sim$1 V/cm, knowing from previous studies [29] that E_t^+ has a centripetal distribution around the cell axis.

(2) Coupling of a transverse $\vec{E}_t$ and a transverse $\vec{B}_t$ magnetic field. A "class 1" systematic effect can also arise from $\vec{E}_t^+$, $\vec{B}_t^+$ or $\vec{E}_t^-$, $\vec{B}_t^-$ couplings. For this reason it is necessary to measure (and, as much as possible, to minimize) the values of B_x^+, B_x^-, B_y^+, and B_y^-, as well as E_x^+, E_x^-, E_y^+, and E_y^-. This is achieved, with the probe tuned to the $7S_{1/2,F=4} \rightarrow 6P_{3/2,F=5}$ hyperfine component, by performing sequences of measurements similar to the PV sequences, except that a "large" transverse magnetic field (1 G) is applied and reversed, along x then along y. The second-order magnetic perturbation of the Stark dichroism of well-defined signature allows us to extract the components of the transverse magnetic fields (see Sec. 5 in [23]), while we exploit an optical rotation signal to extract the transverse electric fields [44].

Table II summarizes the means we use to minimize the field defects. From day to day, only the $\vec{B}_t^+$ field needs to be readjusted in order to be kept at the 2-mG level. The duration of this control is negligible compared with the data acquisition time needed for measuring B_z^-. The same control procedure is performed at the beginning and at the end of the PV sequences on the $7S_{1/2,F=4} \rightarrow 6P_{3/2,F=4}$ transition, for both tilts $\pm\psi$ of the cell. These measurements allow us to evaluate the systematics per milligauss of stray $\vec{B}_t$-field components. The measured values are then combined with the residual $\vec{B}_t$ field values extracted on the $7S_{1/2,F=4} \rightarrow 6P_{3/2,F=5}$ transition (for the same tilt of the cell), to yield the systematics affecting the PV data. On a day-to-day basis, the size of these effects is a few percent of the PV effect. They are affected by a statistical uncertainty small compared to the statistical error on θ^{pv} and could be corrected for when significantly nonzero. But on the average for a given cell, these effects were kept below the percent level, with the exception of one cell (cell No. 4) for which a correction of $\approx 10\%$ was applied to one-third of the data with its uncertainty taken into account. We have no indication that transverse field effects might be a major problem for a future 1% precision measurement.

Besides the estimation of the effects that break the cylindrical symmetry, a test of isotropy on the PV data themselves provides a diagnosis of their presence (see Sec. V C).

C. Possible instrumental defect affecting the orientation of $\hat{\boldsymbol{\epsilon}}_{ex}$

We have considered the possible existence of a tilt θ_0^-, odd under $\vec{E}_l$ reversal, affecting the excitation polarization at the entrance of the Cs cell. Since the direction of $\hat{\epsilon}_{ex}$ determines the direction of the P-conserving gain axes, such an instrumental defect would exactly simulate the PV tilt θ^{pv}. It is therefore crucial to check that the direction of $\hat{\epsilon}_{ex}$ is unaffected by the field reversal. During PV data acquisition, a second polarimeter is used to analyze the excitation polarization using a fraction of the main beam, picked off at the cell entrance (see Fig. 3). Throughout the measurements, θ_0^- remained at or below the noise level, and the global result $\theta_0^- = -0.030 \pm 0.020$ μrad is compatible with zero. This kind of effect might have arisen from electromagnetic interferences resulting from pulsed $\vec{E}_l$ operation.

D. Misreversal of $\vec{E}_l$ combined with polarization defects

A misreversal of $\vec{E}_l$ cannot contribute by itself, but only through a combined effect also involving polarization defects (e.g., imperfect parallelism of $\hat{\epsilon}_{ex}$ and $\hat{\epsilon}_{pr}$). In fact our reconstitution method protects us efficiently against such an effect since we perform the imbalance calibration for both signs of the $\vec{E}_l$ field. As one can check from Eq. (8) below, this method eliminates any field misreversal from the outset. Nevertheless, the defects are kept below the noise level: field misreversal $\leqslant 10^{-3}$ with a digital servo loop and polarization imperfections $\leqslant 10^{-4}$ by preliminary manual corrections based on atomic signals [19] and real-time monitoring. The defects are stable owing to the good optical quality, homogeneity, small birefringence, etc., of the optical components and cell windows, as well as good reproducibility of the insertion of the $\lambda/2$ plates.

V. DATA ACQUISITION AND PROCESSING, CALIBRATIONS AND RESULTS

A. Reconstruction of the PV signal and data acquisition sequences

On an excitation pulse basis, our dual-channel polarimeter provides the imbalance $(S_1 - S_2)/(S_1 + S_2)$ and the probe intensity $I = S_1 + S_2$ for both the amplified and reference pulses. From these signals, two main quantities are formed: the asymmetry

$$A_{LR} \equiv D_{at} = D_{amp} - D_{ref} \tag{5}$$

and the optical density for the probe,

$$\ln(I_{amp}/I_{ref}) = \mathcal{A} + \mathcal{A}_0 . \tag{6}$$

In Eq. (6), $\mathcal{A}_0$ is a small negative contribution to the optical density due to *absorption* of the probe beam by a 6*P* population of known collisional origin [34]. It is measured once at the beginning of data taking, with the excitation beam detuned a few gigahertz away from the forbidden transition. $\mathcal{A}_0$ typically amounts to -4×10^{-2}, whereas $\mathcal{A} \simeq 1$ at resonance in the para-polarization configuration. No such background is detected on A_{LR}.

We also form the ratio

$$\vartheta = A_{LR}/2[\exp(\eta \mathcal{A}) - 1]. \tag{7}$$

This ratio just provides the tilt angle θ of the eigenaxes [Eq. (1)] within a normalization factor close to 1 (or close to the magnification factor when the polarization magnifier is used), eliminated in the calibration procedure measuring the same quantity for the known θ_{cal} angle. Then over the 30 consecutive laser shots corresponding to a given state of the experiment, the program estimates both the means and standard deviations of ϑ and A_{LR} and stores them for the purpose of later analysis. This sequence is repeated for all the states depicted in Table I. For each reversal, the sign of the initial state σ_{cal}, σ_E, σ_{det}, $\sigma_{pr} = \pm 1$ is chosen at random. The complete signature of the APV signal involves an average over all the 2^4 possible states. For a given $f(\sigma)$, we define the average $\langle f(\sigma) \rangle_\sigma = \frac{1}{2}[f(1) + f(-1)]$—i.e., the σ-even part. This implies that $\langle \sigma f(\sigma) \rangle_\sigma = \frac{1}{2}[f(1) - f(-1)]$ yields the σ-odd part. The first determination of the PV calibrated linear dichroism in a given *excitation* polarization state, $i = \{x, y, u, v\}$, involves the construction of the following quantity:

$$\langle G_i \rangle_{A_{LR}} = \theta_{cal} \left\langle \sigma_E \left[\frac{\langle \sigma_{det} A_{LR}(\{\sigma_j\}) \rangle_{\sigma_{det}\sigma_{cal}}}{\langle \sigma_{det} \sigma_{cal} A_{LR}(\{\sigma_j\}) \rangle_{\sigma_{det}\sigma_{cal}}} \right] \right\rangle_{\sigma_E \sigma_{pr}} . \tag{8}$$

A second determination $\langle G_i \rangle_\vartheta$ is obtained by replacing in the above expression A_{LR} by ϑ [Eq. (7)]. Both methods give identical results. Note that an imperfect $\vec{E}_l$ reversal alone leading to an $\vec{E}_l$-odd contribution to $\mathcal{A}$ does not affect either quantity, thus ensuring suppression of systematics due to $\vec{E}_l$ misreversal. However, it can be shown that a contribution to $\mathcal{A}$ that is both E_l-odd and θ_{cal}-odd does not affect $\langle G_i \rangle_{A_{LR}}$ whereas it would alter $\langle G_i \rangle_\theta$. In this particular example, we see that it is instructive to compare the results obtained with both methods. From the point of view of SNR, we noted that in the method using ϑ, it is somewhat more advantageous to evaluate ϑ over one state (30 laser shots) by replacing $\mathcal{A}$ in Eq. (7) by its average over the 30 laser shots: $\overline{\vartheta} = \langle A_{LR}/2(\exp \eta \langle \mathcal{A} \rangle - 1) \rangle$.

Each four-polarization cycle yields two "isotropic values:" $S_{xy} = \frac{1}{2}(G_x + G_y)$ and $S_{uv} = \frac{1}{2}(G_u + G_v)$. The polarization cycles are repeated over $\sim$90 min, providing us with N_{iso} "isotropic values" (typically $N_{iso} = 30$) for a given tilt ψ of the

TABLE III. Main sequences of data acquisition involved in a run, listed in chronological order.

Tilt of the cell	Probe hfs line $7S_F-6P_{3/2,F'}$	Type of measurement	Duration
ψ	$F=4-F'=5$	B_z^- measurement PV-type	~60 min
		and transverse field control	5 min
ψ	$F=4-F'=4$	PV measurement	~90 min
		and transverse field control	5 min
$-\psi$	$F=4-F'=4$	PV measurement	~90 min
		and transverse field control	5 min
$-\psi$	$F=4-F'=5$	B_z^- measurement PV-type	~60 min
		and transverse field control	5 min

cell and repeated for the opposite tilt $-\psi$. For each tilt, the B_z^- correction is also determined as well as the sensitivity to B_t-dependent systematic effects. The main data acquisition sequences are summarized in Table III. This constitutes a so-called run No. k, providing us with an ensemble of $N_k = 2N_{iso}$ PV data. From this ensemble, we deduce an average value m_k and the standard error σ_k. The average m_k represents the calibrated tilt angle of the gain axes having the complete PV signature defined in Table I—i.e., θ_{exp}^{pv}. We accumulated typically 30 such runs using a given cell. The run results are merged with weights $1/\sigma_k^2$ to give a single result per cell. Alternatively, the N_k individual PV data of all runs of all cells are merged into a single ensemble, the same weight being attributed to any individual datum. The results are presented and compared in Sec. V D.

Besides the PV quantities, several other quantities bearing non-PV signatures are constructed from the polarimeter signals, providing us on a short time scale with a wealth of information making possible real-time corrections for defects or drifts during lengthy data acquisition. The most important of these are (a) $\mathcal{A}$ and $A_{LR}(\theta_{cal}\text{-odd})$, which should be kept maximum since they condition the sensitivity (a decrease is generally due to a drop of i_{ex}), (b) asymmetries under $\vec{E}_l$ reversal of $\mathcal{A}$ and $A_{LR}(\theta_{cal}\text{-odd})$, exploited to cancel the field misreversal, (c) reference imbalance of the polarimeter revealing probe polarization defects and/or drift of the difference of the gains between the two channels, and (d) Atomic imbalances: (i) E_l-even and $\sigma_{\rm det}$-odd reveal pump-probe polarization defects; (ii) E_l-odd and $\sigma_{\rm det}$-even reveal parasitic electrical noise.

B. Noise peak rejection and test of PV data rejection

The aim of noise peak rejection is to discard accidental outlying data without truncating the noise distribution. During data acquisition noise blasts which can affect D_{at} are immediately detected: if the standard deviation of the atomic imbalance $\sigma_{D_{at}}$, estimated in one state of the experiment (i.e., over 30 laser shots), happens to exceed 3 times its typical value, the corresponding measurement is ignored and immediately repeated *before the next parameter reversal is performed*. Under normal conditions, such brief events occur with a probability of only a fraction of a percent. In a few cases, this precaution proved useful to eliminate noise not continuously present, but possibly associated with the electric field shots. This was the case of cell No. 3 mentioned later on, in Sec. V E.

In a time-deferred analysis, we eliminate outlying PV data by self-consistent truncation at three standard deviations on the distribution of the PV data accumulated in a given tilt of the cell. The number of rejected data is small ($\leqslant 1\%$, barely larger than what is expected for a standard Gaussian distribution, 2.6×10^{-3}). Avoided laser-mode hops or imperfect plate positioning after insertion are typical possible causes for outlying data. Since the noise distribution is expected and observed to be symmetric, this truncation operation introduces no bias on the data and reduces slightly the standard deviation. It was also performed over the distributions of PV data at the various stages of the analysis—i.e., over the runs in a given cell and over all data merged together.

C. Test of isotropy

The two values of the isotropic part of the E_l-odd linear dichroism, S_{xy} and S_{uv}, that we extract in each four-polarization cycle are found compatible within the noise level, as one expects from considerations of the symmetry of the Stark dipole of the excitation transition [23]. This is observed in individual runs but it is also confirmed by the global analysis of all data [see Eq. (11) below]. The presence of defects breaking the cylindrical symmetry, responsible for *both* “class1” *and* “class 2” systematics is expected to show up as nonzero differences $D_{xy}=\frac{1}{2}(G_x-G_y)$ and $D_{uv}=\frac{1}{2}(G_u-G_v)$. The isotropy test consists in plotting one point of coordinates (D_{xy},D_{uv}) per data set in a Cartesian coordinate system. In conditions of perfect isotropy, the center of gravity of the cloud of points should merge into the origin within the error bars. In [23] we presented a set of data presenting no significant anisotropy. Here, we present (Fig. 10) another set (1126 data points obtained in cell No. 4) analyzed separately for the two opposite signs of the tilt. The anisotropy is clearly apparent in each tilt, with D_{xy} signals of opposite signs. It is reduced over the whole data set. By contrast, the isotropic contributions in both tilts are statistically compatible. In other words, D_{xy} appears much more sensitive than S_{xy} or S_{uv} to the anisotropy induced by the tilt. Referring to [23], we expect the tilt of the cell to give rise to effects of both “class 1” and “class 2,” but for a tilt ψ_x (i.e., a rotation around $\hat{y}$), “class 1” effects would contribute to both D_{xy} and the isotropic parts S_{xy} and S_{uv} with comparable magnitudes [Eqs. (35), (37), (39) and (40) in [23]]. On the other hand, tilt-dependent “class 2” effects cancel out in S_{xy} and S_{uv}, and hence are not a source of systematic effect, but can contribute to both D_{xy} and D_{uv}. On this particular data set, we interpret the value of D_{uv} remaining after averaging over the two tilts (Fig. 10, right graph) by the presence of a residual tilt ψ_y, independent of the $\psi_x/-\psi_x$ reversal. Therefore, this signal is a useful warning indicating a defect but is not the sign of a systematic effect.

Moreover, when the isotropy test is performed on the whole data set, from one cell to another, residual anisotropies tend to compensate. This means that their principal origin is

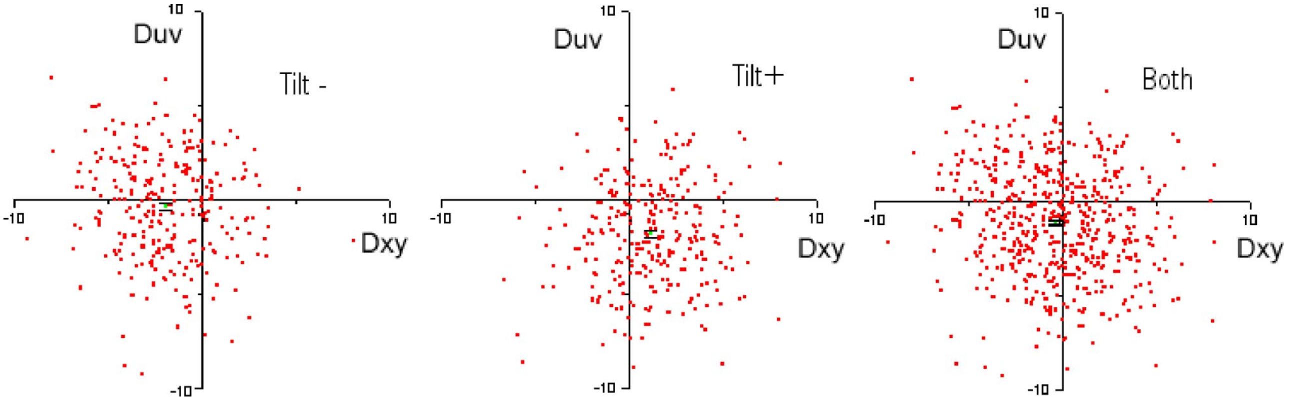

FIG. 10. (Color online) Results of the anisotropy test performed on an ensemble of 1126 data points obtained in cell No. 4. The signals D_{xy} and D_{uv} are analyzed either separately according to the sign of the tilt ψ of the cell (two graphs on the left) or altogether (graph on the right). In this data set there is no tilt-odd contribution to S_{xy} or S_{uv} coming out of noise. See the text for the interpretation.

not in the optical components of the setup but rather arises from slight residual imperfections occuring either during the mounting of each cell inside the electrode assembly or during the fabrication of each individual cell. However, as shown by the final results and the discussion presented hereafter, there is at present no hint of any significant residual systematic effect varying from one cell to the next.

D. Measurement of $\vec{E}_l$ and θ_{cal} for calibrating θ^{pv}

1. Precise in situ measurement of $\vec{E}_l$

To take advantage of the substantial reduction achieved in the statistical uncertainty (see Sec. IV F), we were obliged to reduce also the uncertainty on the magnitude E_l of the field inside the cell, this value being required for a comparison of experiment with theory. For this purpose we changed our calibration method [14]. It can now be conducted in the exact conditions of PV data acquisition: same hyperfine probe transition, excitation energy, and applied potentials. It provides us with reliable results to within a 1% accuracy.

The basic idea relies on the comparison of two optical densities of the vapor at the probe wavelength, the first without any applied electric field and the second in the longitudinal field of magnitude E_l to be measured. They are both proportional to the number of atoms excited in the 7S state, hence to the excitation probability, respectively, $M_1'^2$ and $\beta^2 E_l^2 + M_1'^2$ to within identical proportionality factors (M_1' denotes the 6S-7S transition amplitude [45]). From the optical density ratio we can thus deduce $M_1'^2/\beta^2 E_l^2$—i.e., E_l in terms of the precisely known atomic quantity $M_1'/\beta = 35.1 \pm 0.1$ V/cm [1,10,12]. The optical density is deduced from the polarimeter imbalance resulting from the left-right asymmetry A_{LR} that is associated with the 7S atomic alignment arising from a tilt θ of $\hat{\epsilon}_{ex}$ with respect to $\hat{\epsilon}_{pr}$ (i.e., similar to the calibration signal used for data acquisition). The relation connecting the optical density to A_{LR} can be established precisely by relying on theory [20].

In a first approximation, the result is given by the simple analytical expression $A_{LR} = 2\theta[\exp(\eta_\perp \mathcal{A}_\perp) - 1]$ supposing $\theta \ll 1$ and the ortho configuration with $\eta_\perp = 11/12$ for the $6S_{F=3} - 7S_{F=4} - 6P_{3/2,F=4}$ transition. However, this result is rigorously valid only if one assumes a probe pulse duration t_p long compared with the decay time γ_d^{-1} of the 7S-6$P_{3/2}$ optical dipole and short compared with the 7S lifetime. Actually, in the real conditions of our experiment ($\gamma_d^{-1} = 13.4$ ns, $t_p = 20$ ns, $\tau_{7S} = 47.5$ ns) the deviation with respect to the exponential amplification model, although relatively small ($\leqslant 10\%$), is non-negligible in view of the precision sought. The exact result is deduced from a numerical solution of the exact equations derived in [20] (see Appendix B), using efficient subroutines provided by Mathematica [46].

We have an important reason for choosing the linear dichroism resulting from the 7S atomic alignment as the observable quantity to obtain the value of $\mathcal{A}$ rather than the more direct determination [cf. Eq. (6)] obtained from $\ln(I_{amp}/I_{ref})$: in a zero electric field, differential measurements providing the asymmetry A_{LR} can be performed accurately, while in the same conditions $\mathcal{A}$ (of the order of 2×10^{-4}) is overwhelmed by noise. Moreover, we observe no background superimposed on the atomic alignment ($< 0.3\%$ of the alignment in zero electric field). For this reason, observing the atomic alignment instead of the orientation created by a circularly polarized excitation beam as we did previously [14] corresponds to a real improvement. In addition, for the linear dichroism signal detected on the $6S_{F=3} - 7S_{F=4} - 6P_{3/2,F=4}$ transition, our experimental results confirm that saturation effects are especially weak, as expected in [36].

For practical reasons, for the zero-field measurements (weak optical density), we adjust $\hat{\epsilon}_{ex}$ at 45° from $\hat{\epsilon}_{pr}$ to detect the maximum value of the asymmetry, $A_{LR} = \eta_\perp \mathcal{A}_\perp$, while in the E_l field measurement $\hat{\epsilon}_{ex}$ deviates from $\vec{E}_l \wedge \hat{\epsilon}_{pr}$ by a small known angle $\theta = 12.41 \pm 0.06$ mrad, sequentially reversed from $+\theta$ to $-\theta$. In this way, the imbalance ratio to be measured is of order 70, even though the optical densities differ by a factor of ~ 2000. In this way, we completely avoid possible nonlinearity problems in the detection chain. To eliminate saturation effects, measurements are performed at different levels of the probe-beam intensity to allow for an extrapolation to zero intensity, both with and without the applied electric field since saturation effects depend on the amplification level. The field magnitude is then determined using

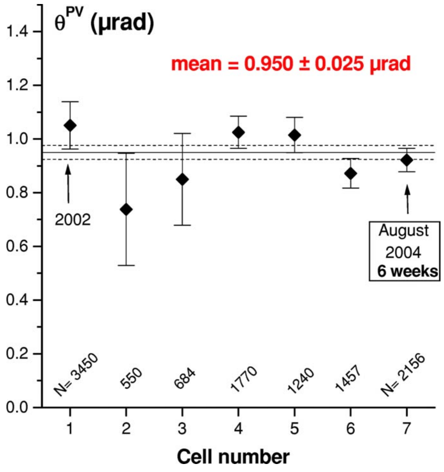

FIG. 11. (Color online) Experimental values of θ^{pv}_{exp} (μrad) obtained in different cells, with their statistical error and the number of isotropic values accumulated in each cell to obtain the result. The solid (dashed) line represents the mean (the statistical error on this mean).

$$E_l^{expt} = \frac{M_1'}{\beta}\left(\sqrt{\frac{\ln[1 + A_{LR}(E = E_l)/2\theta]}{(1 + \epsilon)A_{LR}(E = 0, \theta = \pi/4)}} - 1\right). \qquad (9)$$

Here ϵ is the small quantity expressing the deviation of the exact result with respect to the simple one assuming an exponential-type amplification; it is a function of $\mathcal{A}_\perp(E_l)$ depending on the value taken by the parameter $\gamma_d t_p$. For example, for the realistic values $\gamma_d t_p = 1.49$ and $\mathcal{A}_\perp(E_l) = 0.68$, we obtain $\epsilon = 0.100$. The precision in ϵ is limited by the uncertainty on γ_d, itself a linear function of the cesium atomic density [47]. Allowing for 5% uncertainty in this latter, hence a 3% one in γ_d, the resulting uncertainty in E_l^{expt} is 0.3%. In practical conditions, the precision in E_l is that of the measurements, presently better than 1%. The determination of E_l by this method has been performed in the two types of Cs cells with this level of precision, leading to the results discussed in Sec. III E. The uncertainty in E_l is negligible in comparison with the statistical uncertainty on θ^{pv}_{exp} achieved in each type of cell. In a future work, we plan to investigate the limitations to the signal interpretation which may arise if one wants to push further the precision of this method.

2. Calibration of the polarization-tilt angles

Our measurements of θ^{pv} as well as those of the electric field suppose a precise knowledge of the tilt angles realized by the Faraday rotator in terms of the applied current. Therefore, the calibration of the modulation angle versus the applied Faraday current was repeated several times during the course of our PV measurements. It is done by measuring the mechanical rotation of a Glan prism assembled on a precisely graduated mount which compensates the Faraday rotation. The precision of this calibration, 0.5%, could be improved if need be.

E. Results

Figure 11 summarizes the experimental determinations of θ^{pv}_{exp} obtained cell by cell in seven different Cs cells, with their standard errors and the number of individual isotropic values N_{iso} accumulated to obtain each result. Figure 12 presents the histogram for all the data obtained using the last four cells which have by far the largest statistical weight. The detailed results obtained successively in the different cells are shown in Fig. 13. Since all the measurements were not performed at the same applied potential difference but most of them at a voltage 5% lower, we have made the appropriate correction for renormalizing all results at the same nominal value of E_l, that of Ref. [14], 1619 V/cm. The SNR improvement from the first to the last cell is made conspicuous in Fig. 14 which represents the standard deviation of the distribution of all data accumulated in each cell versus the cell number. Even so, this graph does not make apparent the additional factor of improvement of the SNR per unit of time that results from an increase of the repetition rate.

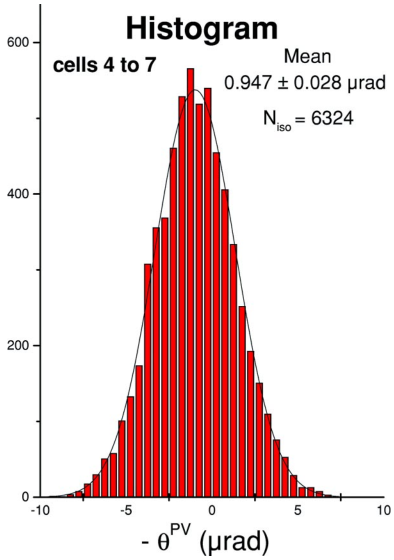

FIG. 12. (Color online) Right: histogram of all the data accumulated in cells 4–7 which have a largely dominant statistical weight. The line represents the Gaussian distribution which has the same mean and standard deviation.

It is important to test the agreement between the results obtained with the seven different cells. More precisely, we check whether the dispersion between the means m_k is compatible with the dispersion σ_k within the measurements performed in each cell. To this end we form the quantity $Q^2 = \Sigma_k[(m - m_k)^2/\sigma_k^2]$ where $m = \Sigma_k(m_k/\sigma_k^2)/(\Sigma_k 1/\sigma_k^2)$ is the weighted average. Q^2 is expected to be sampled from a χ^2 distribution with $\nu = K - 1$ degrees of freedom, $K = 7$ being the number of cells. We find $Q^2/\nu = 7.7/6 = 1.28$ (probability of exceeding 0.26). Such an agreement suggests that possible defects, associated with the preparation of the cells (their geometry and surface properties [48], the filling procedure, etc.), have no detectable effect on our results. Indeed, all the cells were not made of exactly the same material, sapphire/alumina; nor was the machining process identical. All cells had their windows precisely mounted, normal to the tube, except cell No. 2 whose windows were tilted at +3 and −3 mrad towards the horizontal. This allowed us to align $\vec{E}_l$ precisely along the beam direction (see Sec. III D 2) though

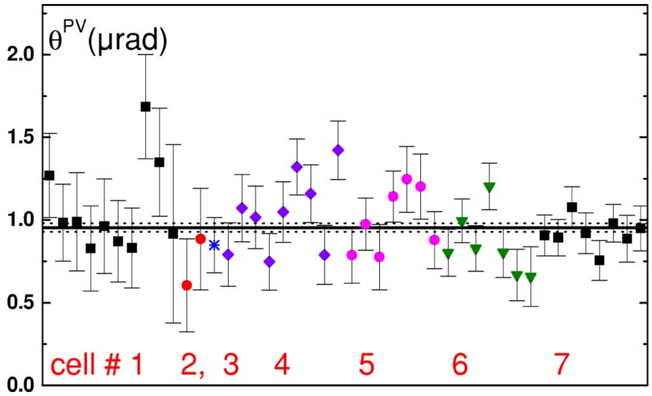

FIG. 13. (Color online) Experimental values of θ_{exp}^{pv} (μrad) with their statistical error obtained in successively accumulated runs (each point corresponds to ≃4 runs), plotted versus the cell numbers chronologically ordered. The solid (dashed) line represents the global mean (the statistical error on this mean).

this did not provide convincing advantages. The possible presence of foreign gas was tested by looking for a broadening of the saturated absorption spectrum of the D_2 resonance line on an auxiliary setup. Only in cell No. 3 could it be observed. This might explain the presence of an unusual short-term noise in this cell, which was rapidly discarded. Note, however, that the value of θ_{exp}^{pv} from this cell still agrees with the average value.

Our present result is

$$\theta_{exp}^{pv}(\mu\text{rad}) = 0.950 \pm 0.025, \quad \text{at } E_l = 1.619 \text{ kV/cm}. \tag{10}$$

This value is nearly unaffected (relative difference 2×10^{-3}) if one attributes the same weight to each individual datum instead of averaging the various runs made with each individual cell and then averaging the results in each cell over the ensemble, with weights $\propto 1/\sigma^2$ at each stage. This gives us confidence that, at the quoted level of precision, our measurements are unaffected by spurious properties varying from one data sample to another. Our data satisfy two other consistency tests.

(i) Agreement between the results obtained with x and y polarizations or u and v, i.e, $S_{xy}=S_{uv}$ within the statistical uncertainty:

$$\frac{1}{2}(S_{xy}^{av} - S_{uv}^{av}) = 0.006 \pm 0.025 \ \mu\text{rad}, \tag{11}$$

(ii) Identity of the results of the two reconstitution methods using either A_{LR} or ϑ [Eqs. (5)–(7)].

Within our uncertainty our result [Eq. (10)] is in excellent agreement with the Boulder one [11], which predicts

$$\theta^{pv}(\mu\text{rad}) = -\frac{\text{Im } E_1^{pv}}{\beta E_l} = 0.962 \pm 0.005,$$

$$\text{at } E_l = 1.619 \text{ kV/cm} \tag{12}$$

for the hyperfine line $6S_{F=3}\rightarrow 7S_{F=4}$ explored during our measurements.

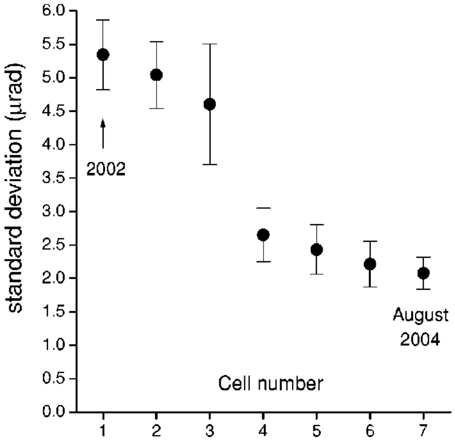

FIG. 14. Right: standard deviation SD of the distribution of the experimental values θ_{exp}^{pv} (μrad) obtained in each individual cell versus the cell numbers chronologically ordered. The error bar on SD is estimated from the dispersion of the SD 's over their distribution in one cell.

Combining our result $\text{Im } E_1^{pv}/\beta = -1.538\pm 0.040$ mV/cm with the value of the vector polarizability determined in [12], $\beta = 27.02\pm 0.08\ a_0^3$, we obtain

$$\text{Im } E_1^{pv}(6S_{F=3} - 7S_{F=4}) = -(0.808 \pm 0.021) \times 10^{-11}|e|a_0. \tag{13}$$

In addition to the statistical uncertainty, the quoted uncertainty includes the uncertainty in the estimation of the registered systematic effects (Sec. IV) as well as in the determination of E_l (Sec. V D). Thanks to our control of systematics and our gain of precision attained in the longitudinal field measurement, the absolute precision in E_1^{pv} reached by our result is limited only by statistics and reaches 2×10^{-13} atomic units. For comparison we note that an absolute precision of 3×10^{-12} atomic units was obtained by the most accurate measurements of E_1^{pv} performed in heavier atoms (Tl, Pb, Bi) where it is 30 times larger [7], but where more difficult atomic physics calculations, presently less precise, are required to extract the weak charge.

VI. RELEVANCE OF ATOMIC PARITY VIOLATION, CONCLUSIONS AND PROSPECTS

A. Goals for further APV measurements

The main goal of atomic parity violation is to provide a determination of the weak nuclear charge Q_W, from the measurement of E_1^{pv} via an atomic physics calculation which now aims at 0.1% precision [49]. In view of present and forthcoming results from high-energy experiments, an important issue concerns the relevance of further improving difficult experiments such as APV measurements. We would like to present arguments in favor of small scale APV experiments.

(1) First we wish to reiterate that APV experiments explore the electroweak (EW) electron-hadron interaction within a range of low momentum transfers q_{at} of 1 MeV or thereabouts in cesium, to be compared with the huge ones explored in collider experiments: 100 GeV at LEP I and LEP

II and 1 TeV at LHC [50]. At low energies, the electroweak amplitude is of the order of $e^2 q_{at}^2 / M_W^2$. In order to compensate for this exceedinly small factor, atomic experiments have to be performed in very special conditions (on a highly forbidden transition in a heavy atom). To obtain relevant information, one has to approach an absolute precision of 10^{-8} in the measurement of a radiative atomic transition LR asymmetry.

(2) For $q_{at} \sim 1$ MeV, the quarks of the atomic nucleus act *coherently*, while at high energies the nucleons are broken into their fundamental constituents: the quarks act then *incoherently*. This is what happens in deep inelastic electron-nucleon scattering, such as the SLAC experiment [51] involving a GeV polarized electron beam colliding against a fixed deuterium target. As a consequence, different combinations of electron-quark PV coupling constants are involved in the LR asymmetries of the two experiments: $\frac{2}{3}C_u^{(1)} - \frac{1}{3}C_d^{(1)}$ at high energies instead of $(2Z+N)C_u^{(1)} + (Z+2N)C_d^{(1)}$ for Q_W. It is easily seen that, in a model-independent analysis, the two experiments delimit nearly orthogonal allowed bands in the $[C_u^{(1)}, C_d^{(1)}]$ plane [1].

(3) Deviations ΔQ_W of Q_W^{expt} from the SM prediction are most often analyzed in the framework of "new physics" models which affect EW interactions *at energies higher than* $M_{Z_0}c^2$ through the existence of gauge bosons heavier than the Z_0, such as, for instance, Kaluza-Klein excitations of the SM gauge bosons [52]. It turns out that ΔQ_W is proportional to the same factor $X = (\pi^2/3) R_\parallel^2 M_{Z_0}^2$ as the deviations from the SM in existing collider experiments, provided that $q^2 R_\parallel^2 \ll 1$, where $R_\parallel \leqslant 1\ \text{TeV}^{-1}$ stands for the compactification radius associated with the additional $d_\parallel$ dimensions of the new physical space for EW gauge fields. A determination of ΔQ_W below the 0.1% level of precision would give constraints on $R_\parallel$, competitive with those of LEP II [53–55]. Furthermore, one can consider models which predict effects undetectable by LEP II results but that would be visible in APV experiments [53,56]. Therefore, a 0.1% accurate Q_W determination could allow one to impose a ~5-TeV limit on the compactification mass $R_\parallel^{-1}$ in a direction possibly invisible to high-energy experiments.

(4) The fact that $q_{at} \sim 1$ MeV allows one to investigate the possible existence of *extra*, *neutral*, *light*, *gauge bosons* more precisely with a mass in the range of a few MeV. Such a drastic modification of EW interactions appears as an alternative explanation for the remarkably intense and narrow γ-ray line emitted from the bulge of our galaxy, close to the energy of 511 keV, which coincides with the electron mass [57,58]. According to this somewhat exotic model, the observed spectrum would result from the annihilation of two *light dark matter particles* (mass $\geqslant 1-2$ MeV) into a pair (e^+, e^-) via the exchange of a light gauge boson U, with a mass of about 10 MeV [59]. In order to reproduce the size of the effects observed experimentally, one has to exclude at a large confidence level an *axial* coupling of the electrons to the new U boson, while such a coupling is the only possible one for *dark particles* which carry no charge. This is where APV comes into play.

The most plausible conclusion to which leads the present value of ΔQ_W [7] is that the U boson couples to the electron as a vector particle with no axial coupling at the 10^{-6} level, while its vector coupling to leptons and quarks are of the same order of magnitude [60]. Thus, the APV measurements provide an empirical justification for a key hypothesis, introduced in the astrophysical model accounting for the 511-keV galactic line.

B. Conclusions and prospects

Our experiment has provided yet another method to measure atomic parity violation in a highly forbidden transition. In the first Cs experiment [9], the signal detected was *the circularly polarized* fluorescence intensity emitted on the $7S_{1/2}$-$6P_{1/2}$ transition. In an early version of their experiment [61], the Boulder group detected the *total* fluorescence intensity emitted in the second step of the 7*S*-6*P*-6*S* cascade. In their final measurements [11], they operated with an atomic beam optically pumped in one hyperfine state. They detected, by scattering of resonance photons, the population of the second hyperfine ground state resulting from excitation of the forbidden transition followed by cascade deexcitation. However, this signal was superimposed on a background (~25%) arising from stray resonant light. In all cases, the LR asymmetry was finally observed via *fluorescence photons* and directly given by the ratio $\text{Im}\, E_1^{pv}/E_1^{Stark}$.

Our new method exploits the amplification by stimulated emission of a resonant probe beam passing through the vapor along the path of the excitation beam for the short time during which the 7*S* atoms have not yet decayed. The polarization of the probe is modified during this propagation in a way which reveals the parity violating LR asymmetry, the key point being that during the propagation of the probe beam through the vapor the LR asymmetry itself is amplified exponentially. Consequently, the measured asymmetry is no longer inversely proportional to the applied electric field, but rather an increasing function of it. Moreover, the detected, differential, signal is directly the LR asymmetry with no background.

During the course of the work presented here, starting from the preliminary results which validated the method [14], we have succeeded in improving the SNR by a factor of 3.5. Our present result, still in agreement with the Boulder result, has now reached a relative accuracy on $\text{Im}\, E_1^{pv}/E_1^{Stark}$ of 2.6% and an absolute precision of 2.5×10^{-8}. We have described the main modifications of the apparatus that contributed to this gain in sensitivity. We have also shown how we can maintain good control of the systematic effects: by making frequent measurements of the B_z field odd under $\vec{E}_l$ reversal and of the transverse $\vec{E}_t$ and $\vec{B}_t$ fields and by suppressing the effect of the tilt of the cell with respect to the common beam axis. In addition, data analysis provides for confidence tests of the results. Of particular relevance is the compatibility of the results obtained in seven different cells which gives a rather good guarantee against systematic effects arising from cell preparation, prone to variations from one cell to another.

To interpret our data, we measured the electric field experienced by the atoms inside the cell. To this end, we have performed the detection of the 7*S* state alignment, *in the* *absence of any electric field*, arising from the magnetic dipole contribution to the 6*S*-7*S* forbidden transition, $\propto M_1^2$, an effect unobserved heretofore. Since the detection of an alignment relies on the existence of hyperfine coupling in the two atomic states connected by the probe transition (the alignment signal cancels out without this coupling), it is free of collisional background and molecular contribution and still more specific to the forbidden transition than an orientation signal is. Therefore, it offers a nice way for extracting E_l from the ratio $(\beta E_l / M_1)^2$ of the alignments measured with and without the field. However, caution was needed to incorporate in the signal analysis existing deviations with respect to a pure exponential-type amplification process.

We find it remarkable that results of APV experiments that involve scattering photons, of only a few eV, by a sample of a few cubic centimeters of dilute atomic vapor, can stand comparison with experiments performed in colliders of the highest energy, for providing a lower limit on the mass of a hypothetical additional neutral boson. In view of the present need for further measurements, underlined above, there are strong incentives to pursue APV measurements exploiting stimulated-emission detection.

(1) Given the difficult task of controlling and measuring systematic effects by the Boulder group [11,22], a cross-check at the 1% level (i.e., 2σ) of the 0.5% Boulder result for the ^{133}Cs $6S_{F=3} \rightarrow 7S_{F=4}$ line by an independent method would constitute a valuable result. Such a statistical accuracy is now within reach with our setup, even if no further SNR improvement were obtained. Among all systematic effects registered so far, nothing indicates that they might have a redhibitory effect at the 1% precision level, which therefore appears as an achievable goal.

(2) As shown in a recent paper [42], asymmetry amplification can provide a considerable enhancement factor in a *transverse* field configuration and a longer interaction length. A cell with special multielectrode design could "restore cylindrical symmetry," despite the application of a transverse $\vec{E}$ field. Then in a quantum-noise-limited measurement a 0.1% statistical precision would be achievable. Increasing further the probe optical gain would seem to be limited by the onset of spontaneous superradiance, but *triggered* superradiance, on the other hand, would come into play as a unique tool for even larger amplification of the asymmetry and possibly even better precision. The motivation for this project, which looks feasible, is encouraged by the recent success of atomic theoretical physicists who were able to reduce their calculation uncertainty to the 0.5% level [4–7] in 2002 and by their considerable efforts now undertaken to arrive at 0.1% accuracy in their many-body perturbation theory calculations [49].

(3) In a cell experiment the required cesium quantity is very small, of order a few milligrams—i.e., several orders of magnitude smaller than the required quantity in an effusive beam APV experiment [22]. This opens the possibility of an APV measurement with ^{135}Cs, a radioactive isotope with a long half lifetime (3×10^6 years). A quantity of 1 mg of ^{135}Cs corresponds to an activity of approximately 4×10^4 Bq ($\approx 1\ \mu$ Ci), so that necessary radioprotection measures should not preclude the feasibility of such an experiment. Measuring APV with two different isotopes, such as ^{135}Cs and ^{133}Cs, would provide the very first experimental test of the nuclear weak-charge dependence on the neutron number. Since the uncertainty resulting from the neutron distribution is expected to be less than 0.1% in cesium [62], the isotopic dependence would offer an alternative interesting way of testing the standard model [63].

(4) An independent measurement of the nuclear anapole moment, obtained from the difference of the E_1^{pv} determinations on two different hyperfine 6*S*-7*S* lines, today looks particularly necessary in view of the apparent inconsistency of the Boulder result with other data relating to parity violating nuclear forces [7,13]. There exists a long-term project aiming at a direct measurement of the nuclear anapole moment by searching for a linear Stark shift of alkali-metal atoms trapped in a cristalline helium matrix of hexagonal symmetry [64]. Even so, today our experiment has already reached a level of sensitivity such that pursuing this goal on the ^{133}Cs 6*S*-7*S* transition appears achievable.

ACKNOWLEDGMENTS

Laboratoire Kastler Brossel is a Unité de Recherche de l'Ecole Normale Supérieure et de l'Université Pierre et Marie Curie, associée au CNRS (UMR 8552). Fédération de recherche du Département de Physique de l'Ecole Normale Supérieure est associée au CNRS (FR 684). We gratefully acknowledge financial support from IN2P3 CNRS, without which this work would not have been possible. We are very grateful to S. Haroche, C. Cohen-Tannoudji, M. Voos, and M. Spiro for solving the administrative imbroglios encountered by our group. We are indebted to M. Himbert, P. Juncar, and their collaborators of BNM-INM for financial help, generous loan of material, and technical advice as well as to V. Croquette from LPS-ENS for always available, efficient help. It has been a pleasure to collaborate (through the support of DRI/CNRS) with D. Sarkisyan and A. Papoyan, from the Research Institute of Ashtarak. Their efforts have been decisive in improving the cells. We also thank S. Sanguinetti for participating with enthusiasm to the modifications of the setup at an early stage. M. Aït Mohand provided help with infinite patience in the tedious task of numerical data analysis. We thank him as well as E. Brezin and F. Zomer for making this possible. We are most grateful to particle physicists M. Davier and J. Iliopoulos for their scientific interest and continuous support. Last but not least, most invaluable, has been our interaction with M.D. Plimmer.

[1] M.-A. Bouchiat and C. Bouchiat, Rep. Prog. Phys. **60**, 1351 (1997).

[2] D. Budker, *Parity Nonconservation in Atoms, Physics Beyond the Standard Model*, Proceedings of the Fifth International WEIN Symposium, edited by P. Herczeg, C. M. Hoffman, and H. V. Klapdor-Kleingrothaus (World Scientific, Singapore, 1999), pp. 418–441.

[3] M.-A. Bouchiat and C. Bouchiat, J. Phys. (Paris) **35**, 899 (1974).

[4] A. Derevianko, Phys. Rev. Lett. **85**, 1618 (2000).

[5] A. I. Milstein and O. P. Sushkov, Phys. Rev. A **66**, 022108 (2002).

[6] V. A. Dzuba, V. V. Flambaum, and J. S. M. Ginges, Phys. Rev. D **66**, 076013 (2002).

[7] J. S. M. Ginges and V. V. Flambaum, Phys. Rep. **397**, 63 (2004).

[8] V. V. Flambaum and I. B. Khriplovich, Sov. Phys. JETP **52**, 835 (1980).

[9] M.-A. Bouchiat, J. Guéna, L. Hunter, and L. Pottier, Phys. Lett. **117**, 358 (1982); J. Phys. (Paris) **47**, 1709 (1986).

[10] M.-A. Bouchiat and J. Guéna, J. Phys. (Paris) **49**, 2037 (1988); C. Bouchiat and C. A. Piketty, *ibid.* **49**, 1851 (1988).

[11] C. S. Wood *et al.*, Science **275**, 1759 (1997).

[12] S. C. Bennett and C. E. Wieman, Phys. Rev. Lett. **82**, 2484 (1999).

[13] C. Bouchiat and C. A. Piketty, Z. Phys. C **49**, 91 (1991).

[14] J. Guéna, D. Chauvat, Ph. Jacquier, E. Jahier, M. Lintz, S. Sanguinetti, A. Wasan, M.-A. Bouchiat, A. V. Papoyan, and D. Sarkisyan, Phys. Rev. Lett. **90**, 143001 (2003).

[15] E. Jahier, J. Guéna, Ph. Jacquier, M. Lintz, M.-A. Bouchiat, and A. V. Papoyan, Appl. Phys. B: Lasers Opt. **71**, 561 (2000).

[16] D. Chauvat *et al.*, Opt. Commun. **138**, 249 (1997).

[17] M.-A. Bouchiat, Ph. Jacquier, M. Lintz, and L. Pottier, Opt. Commun. **56**, 100 (1985).

[18] M.-A. Bouchiat, J. Guéna, Ph. Jacquier, M. Lintz, and M. D. Plimmer, Opt. Commun. **119**, 403 (1995).

[19] J. Guéna, D. Chauvat, Ph. Jacquier, M. Lintz, M. D. Plimmer, and M.-A. Bouchiat, J. Opt. Soc. Am. B **14**, 271 (1997).

[20] C. Bouchiat and M.-A. Bouchiat, Z. Phys. D: At. Mol. Clusters **36**, 105 (1996). Note that in this work the "ortho" and "para" configurations refer to the relative orientation of the excitation and probe transition dipoles, respectively parallel to $\hat{E}_l \wedge \hat{\epsilon}_{ex}$ and $\hat{\epsilon}_{pr}$; hence, *excitation and probe dipoles quasiparallel* correspond to *orthogonal excitation and probe polarizations*.

[21] J. Guéna, D. Chauvat, Ph. Jacquier, M. Lintz, M. D. Plimmer, and M.-A. Bouchiat, Quantum Semiclassic. Opt. **10**, 733 (1998).

[22] C. S. Wood *et al.*, Can. J. Phys. **77**, 7 (1999).

[23] M.-A. Bouchiat, J. Guéna, and M. Lintz, Eur. Phys. J. D **28**, 331 (2004).

[24] D. G. Sarkisyan and A. V. Melkonyan, Prib. Tekh. Eksp. **32**, 202 (1989) [Instrum. Exp. Tech. **32**, 485 (1989)].

[25] M.-A. Bouchiat, J. Guéna, Ph. Jacquier, M. Lintz, and A. Papoyan, Appl. Phys. B: Lasers Opt. **68**, 1109 (1999).

[26] E. Jahier, J. Guéna, Ph. Jacquier, M. Lintz, and M.-A. Bouchiat, Eur. Phys. J. D **13**, 221 (2001).

[27] M.-A. Bouchiat, J. Guéna, Ph. Jacquier, and M. Lintz, Chem. Phys. Lett. **199**, 85 (1992); Opt. Commun. **104**, 157 (1993).

[28] The E_l field is pulsed to prevent the onset of discharges in the vapor.

[29] J. Guéna, E. Jahier, M. Lintz, A. Papoyan, S. Sanguinetti, and M.-A. Bouchiat, Appl. Phys. B: Lasers Opt. **75**, 739 (2002).

[30] B. Bodermann, H. Knöckel, and E. Tiemann, Basics and usage of the program IODINESPEC, Institut für Quantenoptik, Universität Hannover, 2000.

[31] For this offer we are grateful to Emmaüs Laser.

[32] P. Thioulouse, A. Carenco, and R. Guglielmi, IEEE J. Quantum Electron. **17**, 535 (1981).

[33] J. Guéna, Ph. Jacquier, M. Lintz, L. Pottier, M.-A. Bouchiat, and A. Hrisoho, Opt. Commun. **71**, 6 (1989).

[34] There are several nonresonant mechanisms for the direct excitation of a 6*P* population by the excitation pulse. In the present operating conditions (reduction of the dimer density thanks to a high body temperature of the cell, short excitation-probe delay, and large excitation energy ~1.8 mJ), the dominant mechanism is attributable to 6*S*-6*P* Frank-Hertz collisional excitation by the photoelectrons emitted by the "cathode" window and accelerated by the applied longitudinal electric field.

[35] DEI, Model FPX 800, supplied by Armexel, BP 20-92151 Suresnes, France. We are grateful to Y. Le Ruyet for his help and advice on several occasions.

[36] D. Chauvat, J. Guéna, Ph. Jacquier, M. Lintz, and M.-A. Bouchiat, Eur. Phys. J. D **1**, 169 (1998).

[37] S. Sanguinetti, Ph.D. thesis, Université Pierre et Marie Curie and Università di Pisa, 2004, http://tel.ccsd.cnrs.fr/documents/archives0/0/00/67/85/, Sec. 2-3-4.

[38] M. Lintz, J. Guéna, M.-A. Bouchiat, and D. Chauvat, Rev. Sci. Instrum. **76**, 043102 (2005),

[39] Meller Optics, 120 Corliss Street, Providence, RI 02904, USA, www.melleroptics.com

[40] D. G. Sarkisyan, A. S. Sarkisyan, J. Guéna, M. Lintz, and M.-A. Bouchiat, Rev. Sci. Instrum. (to be published), e-print physics/0504020.

[41] E. Lizon and A. Lugrin (private communication).

[42] J. Guéna, M. Lintz, and M.-A. Bouchiat, J. Opt. Soc. Am. B **22**, 21 (2005).

[43] M.-A. Bouchiat, J. Guéna, Ph. Jacquier, M. Lintz, and M. D. Plimmer, Z. Phys. D: At. Mol. Clusters **33**, 89 (1995).

[44] J. Guéna, M. Lintz, and M.-A. Bouchiat (unpublished).

[45] The magnetic dipole amplitude, M_1', includes two contributions: the larger one M_1 arises from many-body and relativistic effects and the other one M_1^{hf}, induced by the nondiagonal hyperfine interaction, is present only in $\Delta F = \pm 1$ transitions (note that the authors of [12] use a sign convention for M_1^{hf}, opposite to our's [10]). Here the E_2 amplitude (see [10]) does not contribute, since, in linear excitation polarization with a quantification axis chosen along $\hat{\epsilon}_{ex} \wedge \hat{k}$, it can only induce $\Delta m_F = \pm 2$ transitions, as opposed to the M_1' amplitude which induces only $\Delta m_F = 0$ transitions; hence, E_2 and M_1' cannot interfere. Moreover, we can neglect $|E_2|^2/|M_1|^2 \ll 10^{-3}$. Note also the absence of any interference term, $\propto \beta E_l M_1'$ in the transition probability, arising from the $\pi/2$ phase difference between the Stark and M_1' amplitudes.

[46] Mathematica, a system for doing mathematics by computer, Wolfram Research.

[47] M.-A. Bouchiat, J. Guéna, Ph. Jacquier, M. Lintz, and L. Pottier, J. Phys. (Paris) **50**, 157 (1989).

[48] Before construction of the cells, the sapphire windows were controlled and rejected in case of birefringence or parallelism defects; then, they were annealed at 1200 °C, a temperature at

which we have checked that reconstruction of the surface takes place. For cell No. 4 and subsequent ones, the tube (either sapphire or alumina ceramics) was also annealed at 1450 °C.

[49] A. Derevianko and E. D. Emmons, Phys. Rev. A **66**, 012503 (2002); C. C. Cannon and A. Derevianko, *ibid.* **69**, 030502(R) (2004).

[50] In this section we use the system of units commonly employed by particle physicists with $\hbar = c = 1$, according to which a length is given by the inverse of a mass or a momentum.

[51] C. Y. Prescott *et al.*, Phys. Lett. **77B**, 347 (1978); **84B**, 524 (1979).

[52] I. Antoniadis *et al.*, JHEP **0105**, 044 (2001).

[53] A. Delgado, JHEP **0001**, 030 (2000).

[54] B. C. Allanach *et al.*, e-print hep-ph/0402295 v5.

[55] C. Bouchiat (unpublished).

[56] K. Cheung and G. Landsberg, Phys. Rev. D **65**, 076003 (2002).

[57] C. Boehm, D. Hooper, J. Silk, M. Casse, and J. Paul, Phys. Rev. Lett. **92**, 101301 (2004).

[58] C. Boehm, P. Fayet, and J. Silk, Phys. Rev. D **69**, 101302(R) (2004).

[59] P. Fayet, Phys. Rev. D **70**, 023514 (2004) and references therein.

[60] C. Bouchiat and P. Fayet, Phys. Lett. B **608**, 87 (2005).

[61] M. C. Noecker, B. P. Masterson, and C. E. Wieman, Phys. Rev. Lett. **61**, 310 (1988).

[62] A. Derevianko and S. Porsev, Phys. Rev. A **65**, 052115 (2002).

[63] E. N. Fortson, Y. Pang, and L. Wilets, Phys. Rev. Lett. **65**, 2857 (1990).

[64] M.-A. Bouchiat and C. Bouchiat, Eur. Phys. J. D **15**, 5 (2001).